

OODFace: Benchmarking Robustness of Face Recognition under Common Corruptions and Appearance Variations

Caixin Kang¹, Yubo Chen¹, Shouwei Ruan¹, Shiji Zhao¹, Ruochen Zhang¹,
 Jiayi Wang², Shan Fu², Xingxing Wei^{1*}

¹ Institute of Artificial Intelligence, Beihang University

² China Academy of Information and Communications Technology

{caixinkang, xxwei}@buaa.edu.cn

Abstract

With the rise of deep learning, facial recognition technology has seen extensive research and rapid development. Although facial recognition is considered a mature technology, we find that existing open-source models and commercial algorithms lack robustness in certain real-world Out-of-Distribution (OOD) scenarios, raising concerns about the reliability of these systems. In this paper, we introduce **OODFace**, which explores the OOD challenges faced by facial recognition models from two perspectives: common corruptions and appearance variations. We systematically design 30 OOD scenarios across 9 major categories tailored for facial recognition. By simulating these challenges on public datasets, we establish three robustness benchmarks: *LFW-C/V*, *CFP-FP-C/V*, and *YTF-C/V*. We then conduct extensive experiments on 19 different facial recognition models and 3 commercial APIs, along with extended experiments on face masks, Vision-Language Models (VLMs), and defense strategies to assess their robustness. Based on the results, we draw several key insights, highlighting the vulnerability of facial recognition systems to OOD data and suggesting possible solutions. Additionally, we offer a unified toolkit that includes all corruption and variation types, easily extendable to other datasets. We hope that our benchmarks and findings can provide guidance for future improvements in facial recognition model robustness.

1. Introduction

In recent years, the rise of deep learning has significantly advanced facial recognition (FR) technology, leading to extensive research and rapid development worldwide. Innovations in loss functions such as SphereFace [30], CosFace [47] and ArcFace [10], have greatly enhanced the efficiency of FR models, achieving unprecedented accuracy under standard conditions. Additionally, the release

*Corresponding authors.

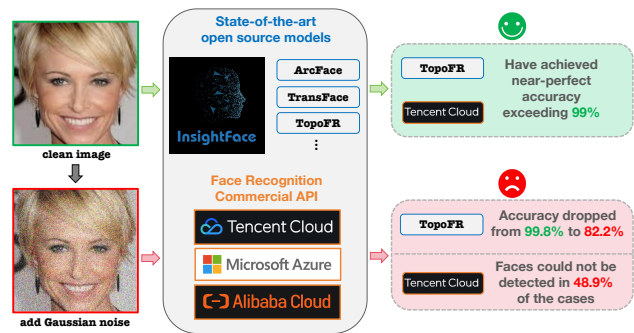


Figure 1. Challenges in FR systems. Simple Gaussian noise poses a threat to the performance of state-of-the-art open-source FR models and commercial FR APIs. (Accuracy tested on LFW.)

of large-scale facial datasets like MS-Celeb-1M [17] and VGGFace2 [6] has further boosted algorithm performance. State-of-the-art open-source algorithms [5, 8, 9, 23] have achieved near-perfect accuracy in FR, while mature commercial APIs from companies like Microsoft, Tencent and Alibaba have enabled the widespread deployment of FR systems in various fields, including security surveillance, identity verification, and financial services, indicating that FR has become a well-established technology.

(Problem statement) Since FR has become a well-established technology, are FR models capable of handling all complex real-world scenarios?

In real-life scenarios, users still encounter issues, such as failing to unlock apartment access during snowy weather or unsuccessful facial recognition for apps that have not been used for a while [2]. To explore the causes, we conduct a simple experiment by adding light Gaussian noise to facial images (potentially introduced during data processing or transmission), as shown in Fig. 1. Although humans can easily recognize the person in both images, we find that state-of-the-art open-source models [9] and the commer-

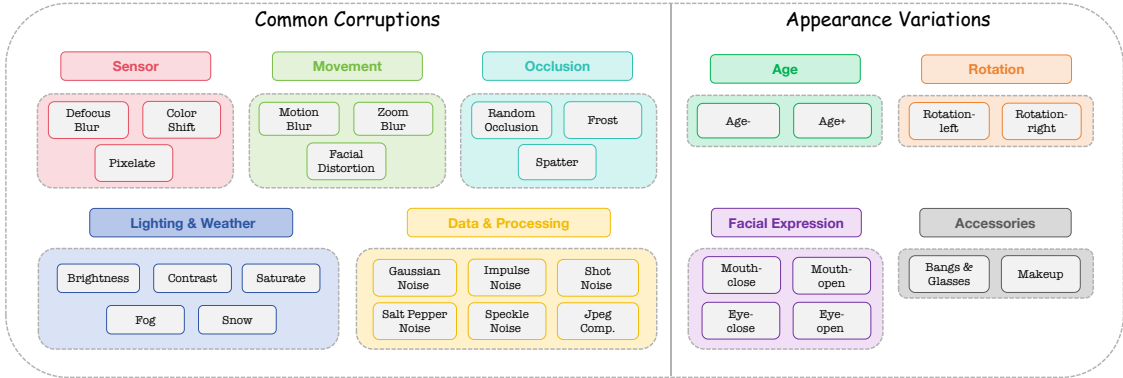


Figure 2. Overview of **OODFace**'s 30 OOD scenarios. OODs are divided into two major categories, common corruptions and appearance variations, further subdivided into 20 and 10 subcategories, each with 5 severity levels.

cial API of Tencent experience a significant drop in performance, with the detection success rate dropping to 82.2%. The API fails to detect faces in 48.9% of the images, disrupting the normal functioning of the FR system.

This indicates that while current FR algorithms perform well under undisturbed conditions, they are still vulnerable to various natural disturbances in real-world applications. Despite the existence of many datasets, such as typical benchmarks [6, 17, 22, 35, 42, 49], most of them focus on ideal conditions. Previous studies have examined the robustness of FR, but they mainly address adversarial perturbations [52], fairness issues [28] or certain categories such as weather [2], occlusion [36, 56]. Thus, comprehensively characterizing challenging samples from diverse real-world Out-of-Distribution (OOD) scenarios and fairly evaluating the natural robustness of existing models within a unified framework remains an open problem.

In this paper, we explore the OOD challenges faced by FR models from the perspectives of common corruptions and appearance variations. We systematically design 30 common OOD scenarios tailored for FR to rigorously assess the OOD robustness of current models. Common corruptions are classified into five categories: Lighting & Weather, Sensor Failures, Motion Errors, Data Processing Corruptions, and Object Occlusion, covering 20 subclasses. Appearance variations are grouped into four categories: Age, Facial Expression, Head Pose, and Accessories, comprising 10 subclasses, covering most real-world disturbances (see Fig. 2). Many of these scenarios, such as Facial Distortion, Random Occlusion, Age, and Accessories, are designed specifically for FR and have not been previously explored by [2, 28, 36, 52, 56]. Following [20], each scenario includes five severity levels, resulting in 150 unique corruptions and variations. By applying these scenarios to standard FR datasets—LFW [22], CFP-FP [42], and YTF [49]—we establish three comprehensive benchmarks for robustness evaluation: LFW-C/V, CFP-C/V, and YTF-C/V, representing common corruptions and appear-

ance variations, respectively. We hope these large-scale OOD datasets can serve as standard benchmarks for fair and comprehensive evaluation of OOD robustness in FR models, facilitating future research in the field.

We conduct extensive experiments to compare the OOD robustness of existing FR models. Specifically, we evaluate 19 open-source models and 3 commercial APIs, covering a variety of loss functions, backbone networks, and model sizes, across the LFW-C/V, CFP-FP-C/V, and YTF-C/V benchmarks. Based on the evaluation results, we find that: 1) Common corruptions robustness is uncorrelated with clean data performance, whereas appearance variations robustness shows the opposite trend; 2) FR models show significant performance drops under common corruptions, with the largest impact from Data & Processing; 3) different FR models show varying sensitivity to different types of OOD scenarios. More discussions are provided in Sec. 5. Additionally, we explore the effectiveness of face masks under OOD conditions and investigate leveraging the generalization capabilities of Vision-Language Models to address OOD challenges. Finally, we examine 10 robust models using *input transformation* [50, 51] and *adversarial training* [32, 53] as potential defense for improving robustness in Appendix F. However, the observed robustness gains are limited. Therefore, despite their widespread use in critical applications, FR models still exhibit vulnerabilities, and enhancing their robustness remains an open challenge.

2. Related Work

2.1. Face Recognition

Facial recognition, a key task in computer vision, has made significant progress in recent years. Early models like DeepFace [44] and FaceNet [41] were the first to demonstrate the power of deep learning for FR tasks. Later, models such as SphereFace [30], CosFace [47], and ArcFace [10], which leverage angular margin-based loss functions, further enhanced feature discriminability. AdaFace [23] introduced an adaptive margin function to

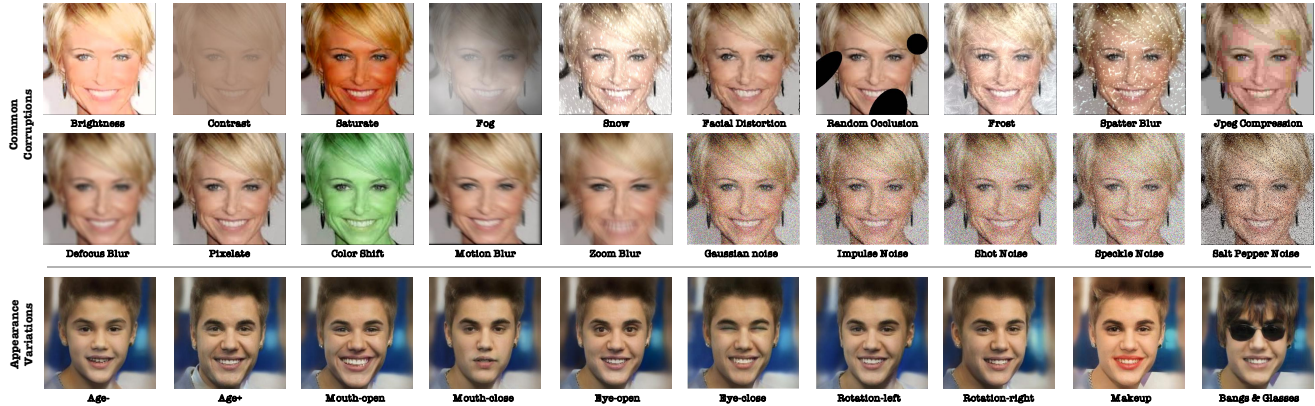


Figure 3. Visualization of 30 subcategories of common corruptions and appearance variations. More results are available in Appendix H.

adjust sample weighting based on image quality, improving performance on low-quality datasets. TransFace [8] focuses on FR by employing a patch-level data augmentation strategy (DPAP) and an entropy-based hard sample mining (EHSM), which preserves facial structure while enhancing sample diversity. The latest TopoFR [9] model incorporates topology alignment and hard sample mining, effectively preserving data structure and improving generalization.

Most state-of-the-art FR models are trained on large datasets like MS-Celeb-1M [17] and VGGFace2 [6], achieving outstanding performance on benchmarks such as LFW [22], CFP [42], YTF [49], and IJB [24, 33, 48], with accuracy often exceeding 99%. Additionally, commercial FR APIs from providers like Tencent, Alibaba, and iFlytek also demonstrate high accuracy.

2.2. Robustness Benchmarks

It is well known that deep learning models lack robustness against adversarial samples [16, 43], common corruptions [12, 20], and other types of distribution shifts [14, 15, 45]. In the field of FR, despite the introduction of many datasets such as LFW [22] and YTF [49], typical benchmarks mainly focus on FR under natural conditions. Some studies have proposed datasets to evaluate model robustness under various conditions, such as facial rotation (frontal-profile) in CFP [42] and age-related attributes in AgeDB [35]. However, due to the high cost of collecting rare data, these datasets cover only a limited range of scenarios. Additionally, certain types of OOD face images are difficult to obtain due to their rarity and specific characteristics, such as sensor failure or age progression, posing challenges for real-world data collection.

A promising approach is to synthesize realistic OODs on clean datasets for benchmarking model robustness. For example, ImageNet-C [20] introduced 15 types of corruptions for image classification, including noise, blur, weather, and digital artifacts. Similar methods have been applied to ob-

ject detection [34], point cloud recognition [38, 58], and autonomous driving [12]. Some works have explored robustness evaluation for FR, but they mainly focus on adversarial perturbations [52] or fairness issues [28]. Given the diverse real-world applications of FR, building a comprehensive robustness evaluation benchmark remains a challenging task.

3. OOD in Face Recognition

We introduce the categories of common corruptions and appearance variations in Sec. 3.1 and Sec. 3.2, respectively, and provide implementation details in Appendix A.

3.1. Common Corruptions

Real-world corruptions in FR arise from diverse application scenarios. Based on this, we classify corruptions into five categories: Lighting & Weather, Sensor, Movement, Data & Processing, and Occlusion. Considering the varied environments of FR applications, we identify 20 distinct types of corruptions across these categories, as illustrated in Fig. 2. We visualize examples of these corruptions in Fig. 3.

Lighting & Weather: Changes in lighting conditions and complex weather are common in FR scenarios, such as variations in daylight, indoor/outdoor lighting, or adverse weather like fog and snow [2]. These conditions can reduce image clarity, blur facial features, or introduce partial occlusions. We categorize these as brightness, contrast, saturation, fog, and snow. Image enhancement techniques [20] are used to simulate realistic weather and lighting effects.

Sensor: Sensors can suffer from internal or external disturbances (e.g., sensor vibrations, lighting conditions [20, 27], reflective surfaces), causing data degradation. Based on prior studies on sensor noise [12, 20], we design three realistic sensor-level corruptions: defocus blur, color shift, and pixelation. Defocus blur simulates the effect of an out-of-focus lens. Color shift alters the overall hue of the image, mimicking color bias due to sensor issues or ambient lighting. Pixelation reduces image detail by compressing it into larger pixel blocks, obscuring facial features.

Movement: Motion is a common cause of image blur, stemming from camera movement or subject motion [12]. We introduce three motion-level corruptions: motion blur, zoom blur, and facial distortion. Motion blur simulates blur from fast motion or camera shake. Zoom blur mimics rapid zooming. Facial distortion simulates unnatural deformation from quick facial movements during image capture.

Data & Processing: During processing, interference can degrade image quality [37]. We simulate this with Gaussian noise, impulse noise, shot noise, speckle noise, salt-and-pepper noise, and JPEG compression. These noises add random perturbations, simulating sensor noise during image acquisition and transmission. JPEG compression simulates image quality loss due to excessive compression.

Occlusion: Occlusion includes random occlusion, frost, and spatter. Random occlusion adds blocks of varying shapes and sizes, mimicking occlusions from objects like hands or hair. Frost, inspired by [20], simulates a white frost-like noise on the camera lens. Spatter simulates quality degradation from raindrops or mud splashes on the lens.

Corruption levels: We follow [20] to define five severity levels for each type of corruption, as shown in Fig. 4. Using Motion Blur as an example, we visualize results from level 1 (mild) to level 5 (extreme).



Figure 4. Visualization of severity levels. **Top:** Motion Blur from level 1 to 5; **Bottom:** Age- from level 1 to 5. Full visual results are available in Appendix H.

3.2. Appearance Variations

Beyond common corruptions, we also consider semantic-level facial variations that may occur in daily life. These are categorized into four groups: Age, Facial Expression, Head Pose, and Accessories, covering 10 unique types of changes as Fig. 2. We provide visual examples in Fig. 3.

Age: Age is a key semantic variable, as facial features change noticeably over time [29]. Using generative facial aging techniques [39], we simulate facial changes across different age stages. These changes involve skin texture, looseness, wrinkles, and overall facial structure.

Facial Expression: Facial expression is another common appearance variation, especially under emotional fluctuations that affect the mouth and eye regions [11]. Using generative models [39], we edit facial expressions to simulate changes like smiling or frowning.

Head Pose: Head pose (or viewpoint) frequently changes in real-life scenarios, particularly when faces are captured

| Models | Venue | Backbone | Loss | Para.(M) | Acc.(%) |
|--------------------|-----------|-----------------|-------------|----------|---------|
| FaceNet [41] | CVPR15 | InceptionResNet | Triplet | 27.9 | 99.2 |
| SphereFace [30] | CVPR17 | Sphere20 | A-Softmax | 28.1 | 98.2 |
| CosFace [47] | CVPR18 | Sphere20 | LMCL | 22.7 | 98.7 |
| ArcFace [10] | CVPR19 | IR-SE50 | ArcFace | 43.8 | 99.5 |
| AdaFace [23] | CVPR22 | IResNet50 | AdaFace | 43.6 | 99.8 |
| ElasticFace [5] | CVPR22 | IResNet100 | ElasticFace | 65.2 | 99.8 |
| TransFace [8] | ICCV23 | ViT-S | ArcFace+ | 86.7 | 99.8 |
| TopoFR [9] | NeurIPS24 | ResNet50 | ArcFace+ | 87.5 | 99.8 |
| MobileFace [7] | ECCV18 | MobileFaceNet | LMCL | 1.2 | 99.5 |
| MobileNet [21] | CVPR17 | MobileNet | LMCL | 3.8 | 99.4 |
| MobileNet-v2 [40] | CVPR18 | MobileNetv2 | LMCL | 2.9 | 99.3 |
| ShuffleNet [57] | CVPR18 | ShuffleNetV1 | LMCL | 1.5 | 99.5 |
| ShuffleNet-v2 [31] | ECCV18 | ShuffleNetV2 | LMCL | 1.8 | 99.2 |
| ResNet50 [10] | CVPR16 | ResNet50 | LMCL | 40.3 | 99.7 |
| Softmax-IR [4] | - | IResNet50 | Softmax | 43.6 | 99.6 |
| SphereFace-IR [30] | - | IResNet50 | A-Softmax | 43.6 | 99.6 |
| AM-IR [46] | - | IResNet50 | AM-Softmax | 43.6 | 99.2 |
| CosFace-IR [47] | - | IResNet50 | LMCL | 43.6 | 99.7 |
| ArcFace-IR [10] | - | IResNet50 | ArcFace | 43.6 | 99.7 |
| iFLYTEK API | - | - | - | - | 98.0 |
| Aliyun API | - | - | - | - | 99.7 |
| Tencent API | - | - | - | - | 99.8 |

Table 1. Tested FR models and commercial APIs.

from various angles by surveillance cameras. Using editing algorithms [39], we modify head orientation to simulate different facial angles, from frontal to side profiles.

Accessory & Makeup: In everyday life, people often wear various accessories that can obscure or alter facial features [36]. Based on [26], we add accessories to the images to simulate real-world accessories occlusions Makeup, especially common in social settings, can visually alter facial features by changing eyebrow shapes, eyeliner, blush, and lip color. We follow [25] to add diverse makeup styles.

Variation Levels: Similar to common corruptions, we define five severity levels for appearance variations (see Fig. 4) For age adjustments, the levels indicate the degree of age reduction or increase. For facial expressions, the levels represent the extent of mouth and eye movements. Head pose levels denote the degree of facial rotation. For accessory additions, the levels are defined as follows: glasses (clear lenses), bang occlusion, glasses (reflective lenses), glasses (clear lenses) + bang, and glasses (reflective lenses) + bang. For the makeup variation, we adopt the styles defined in [25]: Japanese style, Korean style, Retro style, Flashy style, and Smoky-eyes style. Each level represents an increase in perceived appearance interference.

4. OOD Benchmarks

To thoroughly evaluate the robustness of FR models, we establish multiple robustness benchmarks using widely adopted datasets: LFW [22], CFP-FP [42], and YTF [49]. For each dataset, we create two benchmark versions: one for common corruptions (denoted as LFW-C, CFP-C, YTF-C) and one for appearance variations (denoted as LFW-V, CFP-V, YTF-V). Additionally, we offer a unified toolkit that includes all corruptions and variations, easily extendable to other datasets. Below, we detail the datasets, evaluation metrics, and FR models used in our benchmarks.

4.1. LFW-C/V

We first conduct experiments using the LFW [22] dataset, a widely used benchmark in FR. LFW consists of 5,749 identities and 13,233 images, forming 6,000 pairs of face images. We preprocess the entire LFW dataset using MTCNN [54], obtaining aligned images. We then apply 20 types of common corruptions and 10 types of appearance variations. Each includes five levels of severity [20].

Common Corruption Dataset LFW-C. We design LFW-C, a version of the LFW dataset that incorporates common corruptions, to comprehensively evaluate the robustness of FR models under various types and severities of corruption. For each model, we first obtain its performance on the original LFW dataset, denoted as Acc_{clean} . We then re-evaluate the model’s performance under each corruption type c and severity level s in LFW-C, denoted as $Acc_{c,s}$.

We calculate the average corruption robustness among 5 severity levels of the model using the following formula:

$$Acc_{cor} = \frac{1}{|C|} \sum_{c \in C} \frac{1}{5} \sum_{s=1}^5 Acc_{c,s} \quad (1)$$

where c represents all corruption types. To further analyze the degradation of the model under each corruption, we introduce the *Relative Corruption Error (RCE)*, which measures the percentage decrease in performance as follows:

$$RCE_{c,s} = \frac{Acc_{clean} - Acc_{c,s}}{Acc_{clean}}; RCE = \frac{Acc_{clean} - Acc_{cor}}{Acc_{clean}} \quad (2)$$

Appearance Variations Dataset LFW-V. We also design LFW-V, an appearance editing version of the LFW. Similarly, for the LFW-V, we first obtain the Acc_{clean} and then evaluate the model’s performance under each variation category v and severity level s , denoted as $Acc_{v,s}$.

We calculate the average robustness of appearance variations for the model using the following equation:

$$Acc_{var} = \frac{1}{|V|} \sum_{v \in V} \frac{1}{5} \sum_{s=1}^5 Acc_{v,s} \quad (3)$$

where v represents all appearance variations. To further analyze the performance variation of the model under each appearance variations condition, we introduce the *Relative Variations Error (RVE)*, which measures the percentage decrease in performance as follows:

$$RVE_{v,s} = \frac{Acc_{clean} - Acc_{v,s}}{Acc_{clean}}; RVE = \frac{Acc_{clean} - Acc_{var}}{Acc_{clean}} \quad (4)$$

4.2. CFP-C/V

The CFP (Celebrities in Frontal-Profile) [42] dataset consists of frontal and profile images of celebrities. It includes clear frontal and side-view face images, with a total of 500 identities and 7,000 pairs. Following a similar procedure as LFW, we first align all images using MTCNN [54], then apply designed 20 types of common corruptions and 10 types of appearance variations.

Common Corruption Dataset CFP-C. Similarly, CFP-C introduces 20 types of common corruptions into the CFP validation set. These corruptions are applied with five different levels of severity. For each model, we also first compute Acc_{clean} , and then evaluate the model under each corruption type c and severity level s , denoted as $Acc_{c,s}$. We follow the Equation 1 to calculate Acc_{cor} and Equation 2 to compute the *RCE* in a similar manner.

Appearance Variations Dataset CFP-V. We also design CFP-V, an appearance variations version based on the CFP dataset, and calculate Acc_{clean} , $Acc_{v,s}$, Acc_{var} , *RVE* in a comparable format with LFW-V.

4.3. YTF-C/V

The YouTube Faces (YTF) [49] dataset comprises 3,425 YouTube videos from 1,595 subjects (a subset of LFW celebrities). The videos range from 48 to 6,070 frames in length and include 5,000 video pairs and 10 splits. Following [52], we extract the central frame from each video, selecting 5,000 pairs. These images are then preprocessed using MTCNN [54]. We apply our 30 designed complex scenarios, each with five severity levels [20].

Similarly, to evaluate the robustness of FR models against common corruptions and appearance variations, we design two benchmark versions: YTF-C and YTF-V, with the calculation for evaluation metrics being similar to those used in LFW-C/V and CFP-C/V.

4.4. Testing FR Models

Following the setup in [52], to evaluate the robustness of FR systems, we select 19 state-of-the-art FR models, as summarized in Tab. 1. First, we include the open-source models, such as [5, 8, 9, 23, 41]. Second, to investigate the impact of model architecture, we include several models across different backbones, varying in weight size. These include mainstream architectures like ResNet50 [19] and lightweight networks such as MobileFace [7], MobileNet [21], MobileNet-v2 [40], ShuffleNet [57], and ShuffleNet-v2 [31], all trained with LMCL [47] loss. Additionally, we examine the effect of different loss functions by including models based on the same architecture (IResNet50 [10]), optimized using distance-based loss (e.g., Softmax [4]) and angular margin-based losses (e.g., SphereFace [30], AM-Softmax [46], CosFace [47], and ArcFace [10]). To further enrich the evaluation, we also include three commercial API services, though their underlying mechanisms and training data remain unknown.

5. Benchmarking Results and Insights

We present the evaluation results on LFW-C in Sec. 5.1, and LFW-V in Sec. 5.2, and leave the results on CFP-C/V and YTF-C/V in Appendix C and Appendix D. In Sec. 5.3, we discuss commercial API evaluation, followed by ex-

| Models | | Open-source Model Eval | | | | | | | | | | Architecture Eval | | | | | Loss Function Eval | | | | |
|--------------------|-------------------|------------------------|---------|------------|--------------|--------------|--------------|---------|-----------|--------------|------------|-------------------|--------------|------------|---------------|----------|--------------------|---------------|--------------|--------------|------------|
| | | Corruptions | FaceNet | SphereFace | CosFace | ArcFace | ElasticFace | AdaFace | TransFace | TopoFR | MobileFace | MobileNet | MobileNet-v2 | ShuffleNet | ShuffleNet-v2 | ResNet50 | Softmax-IR | SphereFace-IR | Am-IR | CosFace-IR | ArcFace-IR |
| None (clean) | | 99.23 | 98.20 | 98.63 | 99.50 | 99.80 | 99.83 | 99.75 | 99.78 | 99.43 | 99.40 | 99.10 | 99.43 | 99.15 | 99.72 | 99.53 | 99.57 | 99.18 | 99.70 | 99.67 | |
| Lighting & Weather | Brightness | 98.20 | 95.68 | 96.96 | 99.05 | 99.70 | 99.73 | 99.58 | 99.50 | 98.86 | 98.29 | 97.78 | 98.76 | 98.02 | 99.19 | 99.08 | 99.17 | 98.08 | 99.49 | 99.42 | |
| | Contrast | 84.64 | 84.01 | 84.27 | 92.92 | 95.51 | 99.10 | 96.93 | 94.75 | 87.26 | 84.07 | 83.93 | 86.22 | 83.81 | 89.61 | 89.92 | 90.38 | 88.74 | 89.60 | 89.24 | |
| | Saturate | 98.59 | 97.86 | 98.20 | 98.87 | 99.70 | 99.20 | 98.95 | 99.07 | 99.07 | 98.80 | 98.51 | 99.04 | 98.60 | 99.38 | 99.33 | 99.32 | 98.59 | 99.56 | 99.49 | |
| | Fog | 93.25 | 86.10 | 88.30 | 92.56 | 93.38 | 91.02 | 93.10 | 93.02 | 89.69 | 83.59 | 85.45 | 88.42 | 87.44 | 88.61 | 90.43 | 89.41 | 89.21 | 92.30 | 92.18 | |
| | Snow | 90.96 | 87.23 | 91.84 | 96.53 | 97.48 | 98.83 | 97.87 | 96.80 | 93.86 | 89.99 | 91.10 | 92.61 | 92.58 | 93.06 | 94.92 | 93.97 | 94.66 | 96.09 | 96.25 | |
| Sensor | Defocus Blur | 94.30 | 79.71 | 82.12 | 88.31 | 87.98 | 87.34 | 88.70 | 85.53 | 86.16 | 84.78 | 85.29 | 87.30 | 86.29 | 86.73 | 87.65 | 86.18 | 88.67 | 88.98 | 89.10 | |
| | Color Shift | 98.81 | 97.11 | 98.22 | 99.45 | 99.80 | 99.81 | 99.78 | 99.73 | 99.24 | 99.14 | 98.81 | 99.23 | 98.84 | 99.54 | 99.45 | 99.49 | 98.86 | 99.62 | 99.62 | |
| Movement | Pixelate | 98.83 | 94.42 | 96.21 | 98.46 | 99.51 | 99.80 | 99.23 | 98.61 | 98.29 | 97.52 | 96.99 | 98.51 | 98.16 | 99.09 | 98.95 | 98.76 | 97.98 | 99.21 | 99.21 | |
| | Motion Blur | 96.41 | 87.67 | 89.28 | 95.04 | 95.59 | 94.09 | 96.36 | 93.56 | 92.41 | 91.06 | 91.72 | 93.43 | 92.75 | 93.25 | 94.21 | 93.89 | 93.66 | 95.26 | 95.25 | |
| Data & Processing | Zoom Blur | 97.69 | 96.62 | 97.40 | 98.77 | 99.49 | 99.58 | 99.26 | 99.12 | 98.95 | 98.25 | 97.81 | 98.73 | 98.36 | 99.30 | 99.07 | 99.09 | 98.32 | 99.41 | 99.38 | |
| | Facial Distortion | 94.89 | 79.58 | 84.62 | 93.60 | 91.84 | 95.28 | 93.33 | 92.24 | 92.21 | 87.67 | 88.68 | 92.25 | 91.29 | 90.98 | 92.46 | 91.66 | 92.78 | 93.97 | 94.34 | |
| | Gaussian Noise | 87.84 | 73.13 | 80.82 | 93.21 | 87.19 | 87.68 | 88.40 | 82.18 | 84.66 | 75.69 | 77.30 | 76.73 | 82.43 | 84.10 | 81.77 | 80.40 | 89.23 | 88.70 | 87.05 | |
| | Impulse Noise | 89.02 | 72.90 | 81.90 | 94.65 | 90.10 | 90.27 | 90.03 | 84.25 | 85.94 | 77.41 | 78.37 | 77.02 | 82.09 | 84.42 | 83.41 | 82.81 | 90.97 | 91.06 | 88.90 | |
| | Shot Noise | 84.80 | 70.20 | 77.65 | 93.02 | 86.67 | 86.70 | 87.46 | 81.55 | 81.53 | 72.96 | 73.98 | 73.77 | 78.08 | 81.66 | 78.61 | 77.63 | 87.21 | 86.42 | 84.48 | |
| Occlusion | Speckle Noise | 90.67 | 74.61 | 83.65 | 95.90 | 93.53 | 94.23 | 92.99 | 89.79 | 87.61 | 79.00 | 79.45 | 79.97 | 83.66 | 88.01 | 86.27 | 84.54 | 91.36 | 92.25 | 90.41 | |
| | Salt Pepper Noise | 76.74 | 62.82 | 66.06 | 88.90 | 82.51 | 87.13 | 79.20 | 70.70 | 76.15 | 64.35 | 66.89 | 59.54 | 63.54 | 69.04 | 64.73 | 65.23 | 82.50 | 78.36 | 74.51 | |
| | Jpeg Compression | 98.67 | 95.44 | 97.05 | 98.92 | 99.49 | 99.48 | 99.47 | 99.24 | 98.67 | 98.36 | 98.11 | 98.57 | 97.91 | 99.14 | 98.96 | 98.88 | 98.12 | 99.32 | 99.33 | |
| Average | Random Occlusion | 93.74 | 86.13 | 89.07 | 94.58 | 97.36 | 98.43 | 97.38 | 98.10 | 91.73 | 88.89 | 87.63 | 90.94 | 91.21 | 93.24 | 94.05 | 93.56 | 92.73 | 96.10 | 95.22 | |
| | Frost | 90.93 | 83.24 | 89.98 | 94.50 | 94.29 | 96.88 | 94.36 | 93.94 | 93.04 | 88.73 | 89.52 | 92.17 | 91.54 | 92.44 | 93.36 | 92.09 | 93.33 | 94.83 | 94.99 | |
| | Spatter | 91.25 | 89.20 | 92.26 | 96.60 | 98.27 | 98.82 | 98.93 | 98.30 | 94.70 | 90.88 | 92.36 | 93.62 | 92.71 | 93.87 | 96.87 | 96.80 | 95.69 | 98.02 | 97.64 | |

Table 2. Accuracy of 19 FR models on LFW-C, categorized into *Open-source Model Eval*, *Architecture Eval* and *Loss Function Eval*.

tended experiments on face masks in Sec. 5.4 and VLMs in Sec. 5.5. Key findings are summarized by insight block.

5.1. Common Corruptions Evaluation Results

Tab. 2 shows the robustness evaluation of 19 FR models on LFW-C, categorized into *Open-source Model Eval*, *Architecture Eval*, and *Loss Function Eval*. We report the average performance across five levels for each category. It is evident that natural robustness does not strongly correlate with Acc_{clean} . For example, models with high Acc_{clean} (e.g., TopoFR [9]) does not achieve the high Acc_{cor} . In Fig. 5, we further illustrate the *Relative Corruption Error (RCE)* for each model across different corruption categories. Based on these evaluations, we provide the following analysis:

Comparison of Corruption Types. As shown in Tab. 2 and Fig. 5, all corruption types lead to performance degradation in FR models. Among these, Data & Processing has the highest RCE exceeding 20%. Additionally, Occlusion causes substantial performance drops, likely due to the loss of key facial features. On the other hand, most models exhibit negligible degradation under Sensor Corruptions (e.g., color shift, defocus blur), possibly because these corruptions are partially present in natural face datasets.

Insight 1: FR models experience significant performance drops under common corruptions, with the largest impact from Data & Processing, such as Gaussian noise and salt-and-pepper noise.

Comparison of FR Models. While all models experience performance decline, different models show varying sensitivities to specific corruptions. For instance, FaceNet [7] demonstrates robustness against Sensor and Motion corruptions, possibly due to its use of Triplet Loss. AdaFace [23] achieves the best average FR accuracy across all corruptions, attributed to its adaptive margin loss function, which adjusts sample weighting based on image quality, approximated by the feature norm. Meanwhile, ArcFace [23] achieves the highest accuracy in Data & Processing, benefiting from its Angular Margin Loss, which provides robust

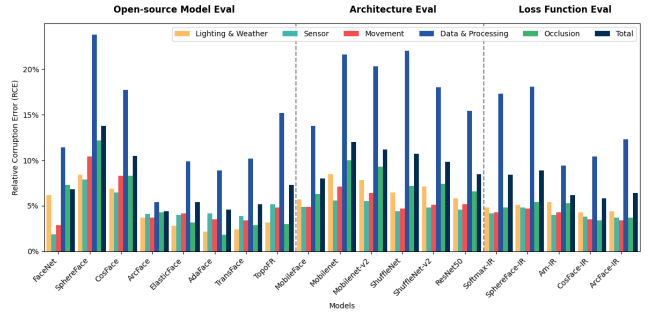


Figure 5. RCE results on LFW-C.

features even under low-resolution or noisy sensor data. **Model Architecture Comparison.** MobileFace [7] achieves the best average robustness with the fewest parameters (1.2M), particularly excelling in the Data & Processing and Occlusion. ResNet50 [19] ranks second in average robustness, showing strong performance in the Lighting & Weather, and Sensor categories.

Loss Function Comparison. Among the loss functions, LMCL [47] achieves the best average results, especially in the Lighting & Weather. This can be attributed to its optimization of inter-class boundaries in the feature space, enhancing model discrimination for similar samples. Additionally, AM-Softmax [46] shows superior robustness in the Data & Processing category.

Insight 2: Different models show varying sensitivity to different types of OOD scenarios. Some models are more robust to specific OOD types but vulnerable to others, indicating that model architecture, loss functions, and training procedures significantly influence performance under specific conditions.

5.2. Appearance Variations Evaluation Results

Tab. 3 presents the variation robustness evaluation of 19 FR models on LFW-V. Overall, the impact of appearance variations is smaller than that of corruptions. Unlike corruptions, robustness against appearance variations is largely correlated with the model’s clean accuracy, consistent with observations in [12, 20]. In Fig. 6, we further illustrate the

| Models Variations | Open-source Model Eval | | | | | | | | | | Architecture Eval | | | | | Loss Function Eval | | | | |
|-------------------|------------------------|------------|---------|---------|-------------|--------------|--------------|--------|------------|-----------|-------------------|------------|---------------|--------------|--------------|--------------------|-------|--------------|--------------|--------------|
| | FaceNet | SphereFace | CosFace | ArcFace | ElasticFace | AdaFace | TransFace | TopoFR | MobileFace | MobileNet | MobileNet-v2 | ShuffleNet | ShuffleNet-v2 | ResNet50 | Softmax-IR | SphereFace-IR | Am-IR | CosFace-IR | ArcFace-IR | |
| None (clean) | 99.23 | 98.20 | 98.63 | 99.50 | 99.80 | 99.83 | 99.75 | 99.78 | 99.43 | 99.40 | 99.10 | 99.43 | 99.15 | 99.72 | 99.53 | 99.57 | 99.18 | 99.70 | 99.67 | |
| Age | Age- | 95.16 | 94.13 | 94.24 | 95.91 | 96.32 | 96.48 | 96.12 | 96.08 | 95.85 | 95.24 | 95.02 | 95.60 | 95.11 | 95.94 | 95.74 | 95.78 | 95.27 | 96.10 | 96.16 |
| | Age+ | 95.22 | 93.85 | 94.67 | 96.00 | 96.39 | 96.60 | 96.39 | 96.19 | 95.86 | 95.52 | 95.34 | 95.88 | 95.39 | 96.16 | 96.14 | 96.13 | 95.43 | 96.30 | 96.42 |
| Facial Expression | Mouth-close | 95.68 | 94.42 | 94.89 | 96.06 | 96.37 | 96.69 | 96.39 | 96.26 | 96.02 | 95.68 | 95.53 | 95.97 | 95.54 | 96.34 | 96.27 | 96.24 | 95.63 | 96.41 | 96.36 |
| | Mouth-open | 95.57 | 94.25 | 94.86 | 96.06 | 96.48 | 96.65 | 96.53 | 96.26 | 95.95 | 95.83 | 95.35 | 96.01 | 95.60 | 96.34 | 96.21 | 96.11 | 95.51 | 96.31 | 96.32 |
| | Eye-close | 94.91 | 94.09 | 94.32 | 95.87 | 96.48 | 96.61 | 96.48 | 96.31 | 95.91 | 95.47 | 95.17 | 95.85 | 95.45 | 96.22 | 96.03 | 95.97 | 95.37 | 96.30 | 96.32 |
| | Eye-open | 95.64 | 94.51 | 95.03 | 96.13 | 96.57 | 96.71 | 96.54 | 96.45 | 96.01 | 95.67 | 95.36 | 96.03 | 95.49 | 96.29 | 96.20 | 96.26 | 95.58 | 96.44 | 96.36 |
| Rotation | Rotation-left | 95.95 | 94.99 | 95.35 | 96.20 | 96.65 | 96.79 | 96.61 | 96.54 | 96.21 | 96.09 | 95.77 | 96.17 | 95.77 | 96.50 | 96.37 | 96.36 | 95.80 | 96.52 | 96.51 |
| | Rotation-right | 95.86 | 94.76 | 95.32 | 96.27 | 96.63 | 96.77 | 96.60 | 96.39 | 96.28 | 96.10 | 95.69 | 96.25 | 95.87 | 96.53 | 96.39 | 96.47 | 95.65 | 96.60 | 96.60 |
| Accessories | Bangs&Glasses | 94.80 | 93.15 | 94.88 | 98.04 | 99.13 | 99.31 | 98.85 | 98.91 | 97.64 | 95.46 | 95.03 | 97.17 | 96.43 | 97.89 | 97.89 | 96.01 | 96.71 | 98.78 | 98.73 |
| | Makeup | 98.32 | 96.60 | 97.42 | 98.97 | 99.70 | 99.70 | 99.54 | 99.58 | 99.02 | 98.55 | 98.32 | 98.86 | 98.38 | 99.29 | 99.16 | 99.29 | 98.50 | 99.46 | 99.42 |
| Average | | 96.03 | 94.81 | 95.42 | 96.82 | 97.32 | 97.47 | 97.26 | 97.16 | 96.74 | 96.27 | 95.97 | 96.66 | 96.20 | 97.02 | 96.90 | 96.92 | 96.24 | 97.17 | 97.17 |

Table 3. Accuracy of 19 FR models on LFW-V, categorized into *Open-source Model Eval*, *Architecture Eval* and *Loss Function Eval*.

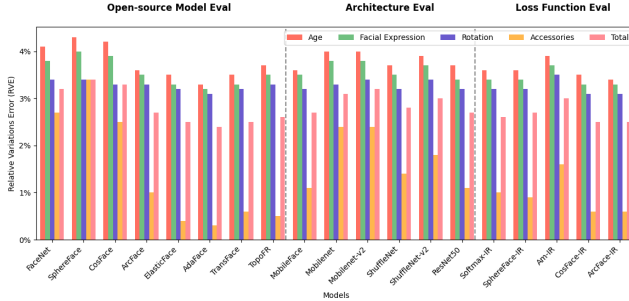


Figure 6. RVE results on LFW-V.

Relative Variation Error (RVE) for each model across variations categories. We provide the following analysis:

Comparison of Variations Types. As shown in Tab. 3 and Fig. 6, appearance variations also degrade model performance, but their impact is generally less severe than corruptions, with the highest RVE around 4%. This could be because, unlike corrupted data, FR models are trained with data that includes redundancy for changes such as age, accessories, and others, making these variations closer to in-distribution data. Additionally, the Accessories have the least overall impact, likely because appearance changes like makeup are superficial and do not alter key facial features. In contrast, age variations have the most significant effect, as aging causes notable changes in facial features, such as increased wrinkles and skin laxity.

Insight 3: The impact of appearance variations is smaller, likely due to redundancy in training data that improves robustness to these changes.

Comparison of FR Models. While models generally maintain high recognition rates under variations, AdaFace [23] achieves the highest average accuracy among open-source models and ranks best across all 10 appearance variations subcategories. This performance can be attributed to the adaptive margin loss function of AdaFace [23], which targets difficult samples, as well as its high clean accuracy.

Model Architecture Comparison. Among the architectures, ResNet50 [19] achieves the best results across all subcategories. This may be due to the deeper network’s stronger feature learning capability, allowing it to effectively capture global features in appearance changes.

Loss Function Comparison. CosFace-IR and ArcFace-IR are tied as the top performers, both achieving an average

| Models Corruptions | Rejection Rate | | | Accepted Samples Accuracy | | | Actual Accuracy | | | |
|--------------------|-------------------|---------|--------------|---------------------------|--------------|--------------|-----------------|--------------|--------------|--------------|
| | Aliyun | iFLYTEK | Tencent | Aliyun | iFLYTEK | Tencent | Aliyun | iFLYTEK | Tencent | |
| None (clean) | 0.00 | 0.00 | 0.00 | 99.65 | 97.99 | 99.75 | 99.65 | 97.99 | 99.75 | |
| L & W | Brightness | 2.02 | 0.23 | 0.67 | 99.73 | 96.48 | 99.60 | 97.71 | 96.25 | 98.93 |
| | Contrast | 35.01 | 17.91 | 4.58 | 99.79 | 96.27 | 99.33 | 64.86 | 79.03 | 94.78 |
| | Saturate | 0.43 | 0.12 | 0.13 | 99.82 | 97.56 | 99.72 | 99.39 | 97.45 | 99.59 |
| | Fog | 44.27 | 7.36 | 17.11 | 99.22 | 92.15 | 97.60 | 55.29 | 85.37 | 80.90 |
| | Snow | 24.12 | 12.68 | 14.38 | 99.43 | 93.32 | 98.75 | 75.45 | 81.49 | 84.55 |
| Sensor | Defocus Blur | 9.55 | 1.20 | 5.60 | 98.58 | 88.56 | 96.79 | 89.17 | 87.49 | 91.37 |
| | Color Shift | 7.59 | 0.38 | 0.85 | 99.78 | 97.31 | 99.71 | 92.20 | 96.94 | 98.86 |
| | Pixelate | 0.55 | 0.02 | 0.08 | 99.75 | 96.45 | 99.63 | 99.20 | 96.43 | 99.55 |
| Movement | Motion Blur | 4.26 | 0.60 | 1.20 | 99.39 | 93.62 | 98.90 | 95.15 | 93.06 | 97.71 |
| | Zoom Blur | 1.12 | 0.03 | 2.76 | 99.70 | 96.54 | 99.36 | 98.58 | 96.51 | 96.62 |
| | Facial Distortion | 12.71 | 13.45 | 7.84 | 98.03 | 87.96 | 96.81 | 85.57 | 76.13 | 89.22 |
| D & P | Gaussian Noise | 89.96 | 71.75 | 48.87 | 99.17 | 91.65 | 95.94 | 9.95 | 25.89 | 49.05 |
| | Impulse Noise | 84.01 | 58.37 | 33.47 | 99.37 | 93.21 | 97.01 | 15.89 | 38.80 | 64.54 |
| | Shot Noise | 93.74 | 84.76 | 63.05 | 97.06 | 88.04 | 93.62 | 6.07 | 13.41 | 34.59 |
| | Speckle Noise | 81.10 | 72.85 | 49.06 | 99.12 | 91.31 | 96.29 | 18.73 | 24.79 | 49.05 |
| | Salt Pepper Noise | 100.00 | 98.95 | 86.03 | 0.00 | 90.48 | 66.59 | 0.00 | 0.95 | 9.30 |
| | Jpeg Compression | 0.54 | 0.03 | 0.13 | 99.71 | 96.30 | 99.56 | 99.18 | 96.27 | 99.43 |
| Occlusion | Random Occlusion | 39.91 | 29.54 | 40.36 | 97.86 | 86.87 | 98.77 | 58.81 | 61.21 | 58.91 |
| | Frost | 62.80 | 39.99 | 19.35 | 99.06 | 92.31 | 97.95 | 36.85 | 55.40 | 79.00 |
| | Spatter | 12.49 | 3.36 | 3.18 | 99.73 | 94.65 | 99.33 | 87.27 | 91.47 | 96.17 |
| Average | 35.31 | 25.68 | 19.94 | 94.47 | 93.29 | 96.71 | 64.27 | 69.72 | 78.61 | |

Table 4. Accuracy of commercial APIs on LFW-C. Due to a large percentage of images being rejected, we report “Rejection Rate,” “Accepted Samples Accuracy,” and “Actual Accuracy.”

accuracy of 97.17%. This can be attributed to the design of LMCL [47] and ArcFace [10] losses, which enhance robustness to complex variations. Additionally, their high clean accuracy suggests that these models effectively learn facial representations, enabling them to maintain capabilities when facing appearance changes.

Insight 4: Model robustness against common corruptions does not fully correlate with clean data performance. Even models that excel on clean data may struggle with certain corruptions. In contrast, robustness to appearance variations is strongly correlated with clean data performance.

5.3. Commercial API Evaluation Results

We evaluate the robustness of three commercial FR services (Aliyun, iFLYTEK, and Tencent) on LFW-C and LFW-V. The underlying mechanisms and training data of these APIs are entirely unknown to us. We follow their original threshold ranges and determine the optimal threshold for each dataset. The results are shown in Tab. 4 and Tab. 5.

Common Corruptions Evaluation. For LFW-C, our first observation is that although the designed corruptions appear mild and have minimal impact on human recognition, they significantly impair the performance of commercial FR systems, often returning “No face detected.” Based on this, we compute the *Rejection Rate (RR)*, representing the proportion of rejected samples. We find that nearly all categories of corruption have cases where the algorithm fails, with the

| Models Variations | | Accuracy | | |
|-------------------|----------------|----------|---------|---------|
| | | Aliyun | iFLYTEK | Tencent |
| None (clean) | | 99.65 | 97.99 | 99.75 |
| Age | Age- | 96.60 | 93.47 | 96.45 |
| | Age+ | 96.60 | 93.50 | 96.59 |
| Facial Expression | Mouth-close | 96.67 | 93.80 | 96.47 |
| | Mouth-open | 96.55 | 93.68 | 96.55 |
| | Eye-close | 96.71 | 93.23 | 96.64 |
| | Eye-open | 96.67 | 94.10 | 96.72 |
| Rotation | Rotation-left | 96.67 | 94.23 | 96.71 |
| | Rotation-right | 96.71 | 94.10 | 96.67 |
| Accessories | Bangs&Glasses | 98.06 | 93.91 | 98.85 |
| | Makeup | 99.13 | 96.60 | 99.28 |
| Average | | 97.27 | 94.42 | 97.33 |

Table 5. Accuracy of 3 commercial APIs on LFW-V.

most significant impact in the Data & Processing category, especially for Salt-and-Pepper Noise, where Aliyun’s API completely fails and gains 100.00% RR. We also compute *Accepted Samples Accuracy (ASA)* and *Actual Accuracy (AA)*, representing the success rate among accepted samples and the overall samples, respectively. While Aliyun’s ASA is relatively high, this is due to its high RR, resulting in a low proportion of accepted samples. Ultimately, Tencent’s API achieves the best RR, highest ASA, and AA, but there is still a noticeable decline in accuracy compared to clean data. Given the substantial detection rejection rates, we conclude that current FR systems need significant improvements in robustness against corruption.

Appearance Variations Evaluation. For LFW-V, no detection rejection occurs as seen in LFW-C, so we report the direct accuracy results. Appearance variations also cause performance degradation, but the impact is smaller compared to corruptions. Among the APIs, Tencent achieves the highest average accuracy, while Aliyun performs better in the Age and Facial Expression. The robustness of these services remains highly correlated with their clean performance, aligning with the conclusions in Sec. 5.2.

Insight 5: Faces with several corruption types fail to be detected by APIs, causing FR systems to malfunction in several OOD scenarios, highlighting the vulnerability of commercial FR systems.

5.4. Extended Experiments on Face Masks

In the field of FR, face masks typically refer to physical disguises used to deceive or obscure the identity of the wearer, preventing the system from accurately recognizing the individual [55]. Masks can replicate the appearance of a real face, thereby bypassing the system’s security measures. As an extension, we conduct physical experiments on masks, creating five different types made from various materials, as shown in Fig. 7. In the experiments, we first test whether the masks could be correctly identified, and then further explore the impact of corruptions and variations on recognition. Our findings indicate that masks are also affected by OOD scenarios, exhibiting a different category of performance degradation compared to real faces. We provide additional experimental data and further analysis in Appendix E, along with details of the mask fabrication process.



Figure 7. Display of face masks. We create 5 types of masks to test the impact of OOD cases on FR.

Insight 6: Face masks are also affected by OOD scenarios, exhibiting a different performance degradation trend compared to real faces.

5.5. Extended Experiments on VLMs

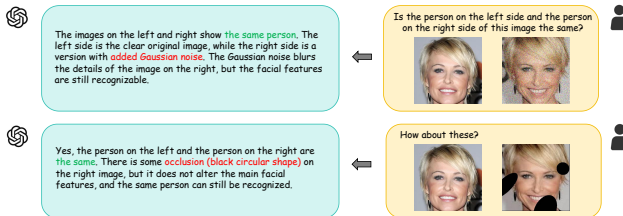


Figure 8. Testing GPT-4o mini for FR. GPT-4o mini demonstrates robust FR capabilities. (More results in Appendix G.)

To explore better solutions for OOD scenarios in FR, we investigate the use of Vision-Language Models (VLMs) for FR, a previously unexplored approach. As shown in Fig. 8, we find that GPT-4o-mini [1] demonstrates robust FR capabilities and can identify specific types of corruption present in the images, suggesting that VLMs could be a solution to the challenge of OOD data.

Insight 7: VLMs can compare facial similarities even in OOD scenarios, suggesting that leveraging the generalization capabilities of large models could be a promising solution for handling OOD cases.

5.6. Extended Experiments on Potential Defenses

We further explore potential defenses for improving robustness in Appendix F. Following [52], we test 10 robust models using *input transformation* such as R&P [50], Bit-Red [51], and *adversarial training* such as PGD-AT [32], TRADES [53]. However, the improvements are limited.

Insight 8: Existing defense strategies fail to address OOD scenarios, and enhancing FR robustness remains an open challenge for future research.

6. Conclusion

In this paper, we introduce **OODFace**, a comprehensive benchmark for OOD robustness in FR, systematically designed with 20 common corruptions across 5 categories and 10 appearance variations across 4 categories. By augmenting public datasets, we establish three robustness benchmarks: LFW-C/V, CFP-FP-C/V, and YTF-C/V. We conduct extensive evaluations on 19 FR models and 3 commercial APIs, along with additional experiments towards face

masks, VLMs, and defense strategies. We hope that our comprehensive benchmarks, detailed analysis, and insightful findings will aid in understanding the robustness of FR models against OOD scenarios, and provide valuable guidance for future improvements in FR model robustness.

References

- [1] Josh Achiam, Steven Adler, Sandhini Agarwal, Lama Ahmad, Ilge Akkaya, Florencia Leoni Aleman, Diogo Almeida, Janko Altenschmidt, Sam Altman, Shyamal Anadkat, et al. Gpt-4 technical report. *arXiv preprint arXiv:2303.08774*, 2023. 8
- [2] Md Manjurul Ahsan, Yueqing Li, Jing Zhang, Md Tanvir Ahad, and Kishor Datta Gupta. Evaluating the performance of eigenface, fisherface, and local binary pattern histogram-based facial recognition methods under various weather conditions. *Technologies*, 9(2):31, 2021. 1, 2, 3
- [3] Bethgelab. Imagecorruptions, 2024. Accessed: 2024-11-21. 1, 2
- [4] Christopher M. Bishop. *Pattern Recognition and Machine Learning*. Springer, 2006. 4, 5
- [5] Fadi Boutros, Naser Damer, Florian Kirchbuchner, and Arjan Kuijper. Elasticface: Elastic margin loss for deep face recognition. In *Proceedings of the IEEE/CVF conference on computer vision and pattern recognition*, pages 1578–1587, 2022. 1, 4, 5
- [6] Qiong Cao, Li Shen, Weidi Xie, Omkar M Parkhi, and Andrew Zisserman. Vggface2: A dataset for recognising faces across pose and age. In *2018 13th IEEE international conference on automatic face & gesture recognition (FG 2018)*, pages 67–74. IEEE, 2018. 1, 2, 3
- [7] Sheng Chen, Yang Liu, Xiang Gao, and Zhenhua Han. Mobilefacenets: Efficient cnns for accurate real-time face verification on mobile devices. In *Chinese Conference on Biometric Recognition (CCBR)*, pages 428–438. Springer, 2018. 4, 5, 6
- [8] Jun Dan, Yang Liu, Haoyu Xie, Jiankang Deng, Haoran Xie, Xuansong Xie, and Baigui Sun. Transface: Calibrating transformer training for face recognition from a data-centric perspective. In *Proceedings of the IEEE/CVF international conference on computer vision*, pages 20642–20653, 2023. 1, 3, 4, 5
- [9] Jun Dan, Yang Liu, Jiankang Deng, Haoyu Xie, Siyuan Li, Baigui Sun, and Shan Luo. Topofr: A closer look at topology alignment on face recognition. *arXiv preprint arXiv:2410.10587*, 2024. 1, 3, 4, 5, 6
- [10] Jiankang Deng, Jia Guo, Niannan Xue, and Stefanos Zafeiriou. Arcface: Additive angular margin loss for deep face recognition. In *Proceedings of the IEEE/CVF conference on computer vision and pattern recognition*, pages 4690–4699, 2019. 1, 2, 4, 5, 7
- [11] Anagha S Dhavalikar and RK Kulkarni. Face detection and facial expression recognition system. In *2014 International Conference on Electronics and Communication Systems (ICECS)*, pages 1–7. IEEE, 2014. 4
- [12] Yinpeng Dong, Caixin Kang, Jinlai Zhang, Zijian Zhu, Yikai Wang, Xiao Yang, Hang Su, Xingxing Wei, and Jun Zhu. Benchmarking robustness of 3d object detection to common corruptions. In *Proceedings of the IEEE/CVF Conference on Computer Vision and Pattern Recognition*, pages 1022–1032, 2023. 3, 4, 6
- [13] Gintare Karolina Dziugaite, Zoubin Ghahramani, and Daniel M Roy. A study of the effect of jpg compression on adversarial images. *arXiv preprint arXiv:1608.00853*, 2016. 5
- [14] Robert Geirhos, Jörn-Henrik Jacobsen, Claudio Michaelis, Richard Zemel, Wieland Brendel, Matthias Bethge, and Felix A. Wichmann. Generalisation in humans and deep neural networks. *Advances in Neural Information Processing Systems (NeurIPS)*, 2018. 3
- [15] Robert Geirhos, Patrick Rubisch, Claudio Michaelis, Matthias Bethge, Felix A. Wichmann, and Wieland Brendel. Imagenet-trained cnns are biased towards texture; increasing shape bias improves accuracy and robustness. In *International Conference on Learning Representations (ICLR)*, 2019. 3
- [16] Ian J. Goodfellow, Jonathon Shlens, and Christian Szegedy. Explaining and harnessing adversarial examples. *International Conference on Learning Representations (ICLR)*, 2015. 3
- [17] Yandong Guo, Lei Zhang, Yuxiao Hu, Xiaodong He, and Jianfeng Gao. Ms-celeb-1m: A dataset and benchmark for large-scale face recognition. In *Computer Vision–ECCV 2016: 14th European Conference, Amsterdam, The Netherlands, October 11–14, 2016, Proceedings, Part III 14*, pages 87–102. Springer, 2016. 1, 2, 3
- [18] Erik Härkönen, Aaron Hertzmann, Jaakko Lehtinen, and Sylvain Paris. Ganspace: Discovering interpretable gan controls. *Advances in neural information processing systems*, 33:9841–9850, 2020. 3, 4
- [19] Kaiming He, Xiangyu Zhang, Shaoqing Ren, and Jian Sun. Deep residual learning for image recognition. *Proceedings of the IEEE Conference on Computer Vision and Pattern Recognition (CVPR)*, pages 770–778, 2016. 5, 6, 7
- [20] Dan Hendrycks and Thomas Dietterich. Benchmarking neural network robustness to common corruptions and perturbations. *arXiv preprint arXiv:1903.12261*, 2019. 2, 3, 4, 5, 6
- [21] Andrew G Howard, Menglong Zhu, Bo Chen, Dmitry Kalenichenko, Weijun Wang, Tobias Weyand, Marco Andreetto, and Hartwig Adam. Mobilenets: Efficient convolutional neural networks for mobile vision applications. *arXiv preprint arXiv:1704.04861*, 2017. 4, 5
- [22] Gary B Huang, Marwan Mattar, Tamara Berg, and Eric Learned-Miller. Labeled faces in the wild: A database for studying face recognition in unconstrained environments. In *Workshop on faces in 'Real-Life' Images: detection, alignment, and recognition*, 2008. 2, 3, 4, 5
- [23] Minchul Kim, Anil K Jain, and Xiaoming Liu. Adaface: Quality adaptive margin for face recognition. In *Proceedings of the IEEE/CVF conference on computer vision and pattern recognition*, pages 18750–18759, 2022. 1, 2, 4, 5, 6, 7
- [24] Brendan F Klare, Joshua C Klontz, and Anil K Jain. Pushing the frontiers of unconstrained face detection and recognition:

- Iarpa janus benchmark a. In *Proceedings of the IEEE Conference on Computer Vision and Pattern Recognition (CVPR)*, pages 1931–1939, 2015. 3
- [25] Tingting Li, Ruihe Qian, Chao Dong, Si Liu, Qiong Yan, Wenwu Zhu, and Liang Lin. Beautygan: Instance-level facial makeup transfer with deep generative adversarial network. In *Proceedings of the 26th ACM international conference on Multimedia*, pages 645–653, 2018. 4
- [26] Xinyang Li, Shengchuan Zhang, Jie Hu, Liujuan Cao, Xiaopeng Hong, Xudong Mao, Feiyue Huang, Yongjian Wu, and Rongrong Ji. Image-to-image translation via hierarchical style disentanglement. In *Proceedings of the IEEE/CVF conference on computer vision and pattern recognition*, pages 8639–8648, 2021. 4
- [27] Zhiqi Li, Wenhai Wang, Hongyang Li, Enze Xie, Chonghao Sima, Tong Lu, Yu Qiao, and Jifeng Dai. Bevformer: Learning bird’s-eye-view representation from multi-camera images via spatiotemporal transformers. In *European conference on computer vision*, pages 1–18. Springer, 2022. 3
- [28] Li Lin, Xin Wang, Shu Hu, et al. Ai-face: A million-scale demographically annotated ai-generated face dataset and fairness benchmark. *arXiv preprint arXiv:2406.00783*, 2024. 2, 3
- [29] Haibin Ling, Stefano Soatto, Narayanan Ramanathan, and David W Jacobs. A study of face recognition as people age. In *2007 IEEE 11th International Conference on Computer Vision*, pages 1–8. IEEE, 2007. 4
- [30] Weiyang Liu, Yandong Wen, Zhiding Yu, Ming Li, Bhiksha Raj, and Le Song. Sphreface: Deep hypersphere embedding for face recognition. In *Proceedings of the IEEE conference on computer vision and pattern recognition*, pages 212–220, 2017. 1, 2, 4, 5
- [31] Ningning Ma, Xiangyu Zhang, Hai-Tao Zheng, and Jian Sun. Shufflenet v2: Practical guidelines for efficient cnn architecture design. In *Proceedings of the European Conference on Computer Vision (ECCV)*, pages 116–131, 2018. 4, 5
- [32] Aleksander Mądry, Aleksandar Makelov, Ludwig Schmidt, Dimitris Tsipras, and Adrian Vladu. Towards deep learning models resistant to adversarial attacks. *stat*, 1050(9), 2017. 2, 8, 5
- [33] Brian Maze, Joshua Adams, J Ross Duncan, Nathan Kalka, Tim Miller, Charles Otto, Karthik Jain, Wayne Niggel, John Anderson, James Cheney, et al. Iarpa janus benchmark-c: Face dataset and protocol. In *2018 International Conference on Biometrics (ICB)*, pages 158–165, 2018. 3
- [34] Claudio Michaelis, Benjamin Mitzkus, Robert Geirhos, Evgenia Rusak, Oliver Bringmann, Alexander S. Ecker, Matthias Bethge, and Wieland Brendel. Benchmarking robustness in object detection: Autonomous driving when winter is coming. In *Advances in Neural Information Processing Systems (NeurIPS)*, 2019. 3
- [35] Stylianos Moschoglou, Athanasios Papaioannou, Christos Sagonas, Jiankang Deng, Irene Kotsia, and Stefanos Zafeiriou. Agedb: the first manually collected, in-the-wild age database. In *proceedings of the IEEE conference on computer vision and pattern recognition workshops*, pages 51–59, 2017. 2, 3
- [36] Pedro C Neto, João Ribeiro Pinto, Fadi Boutros, Naser Damer, Ana F Sequeira, and Jaime S Cardoso. Beyond masks: On the generalization of masked face recognition models to occluded face recognition. *IEEE Access*, 10: 86222–86233, 2022. 2, 4
- [37] Preena Prasad, J Anitha, and Divapriya Anil. A systematic review of noise types, denoising methods, and evaluation metrics in images. In *2023 IEEE International Conference on Recent Advances in Systems Science and Engineering (RASSE)*, pages 1–9. IEEE, 2023. 4
- [38] Zhiyu Ren, Ziyu Liu, Shijie Han, Yiming Li, Yao Zhao, Nicu Sebe, and Wei Wang. Benchmarking and analyzing point cloud classification under corruptions. In *Proceedings of the IEEE/CVF Conference on Computer Vision and Pattern Recognition (CVPR)*, 2022. 3
- [39] Daniel Roich, Ron Mokady, Amit H Bermano, and Daniel Cohen-Or. Pivotal tuning for latent-based editing of real images. *ACM Transactions on graphics (TOG)*, 42(1):1–13, 2022. 4, 2, 3
- [40] Mark Sandler, Andrew Howard, Menglong Zhu, Andrey Zhmoginov, and Liang-Chieh Chen. Mobilenetv2: Inverted residuals and linear bottlenecks. In *Proceedings of the IEEE Conference on Computer Vision and Pattern Recognition (CVPR)*, pages 4510–4520, 2018. 4, 5
- [41] Florian Schroff, Dmitry Kalenichenko, and James Philbin. Facenet: A unified embedding for face recognition and clustering. In *Proceedings of the IEEE conference on computer vision and pattern recognition*, pages 815–823, 2015. 2, 4, 5
- [42] Soumyadip Sengupta, Jun-Cheng Chen, Carlos Castillo, Vishal M Patel, Rama Chellappa, and David W Jacobs. Frontal to profile face verification in the wild. In *2016 IEEE winter conference on applications of computer vision (WACV)*, pages 1–9. IEEE, 2016. 2, 3, 4, 5
- [43] Christian Szegedy, Wojciech Zaremba, Ilya Sutskever, Joan Bruna, Dumitru Erhan, Ian Goodfellow, and Rob Fergus. Intriguing properties of neural networks. *International Conference on Learning Representations (ICLR)*, 2014. 3
- [44] Yaniv Taigman, Ming Yang, Marc’ Aurelio Ranzato, and Lior Wolf. Deepface: Closing the gap to human-level performance in face verification. In *Proceedings of the IEEE Conference on Computer Vision and Pattern Recognition (CVPR)*, pages 1701–1708, 2014. 2
- [45] Rohan Taori, Achal Dave, Vaishaal Shankar, Nicholas Carlini, Benjamin Recht, and Ludwig Schmidt. Measuring robustness to natural distribution shifts in image classification. *Advances in Neural Information Processing Systems (NeurIPS)*, 2020. 3
- [46] Feng Wang, Jian Cheng, Weiyang Liu, and Haijun Liu. Additive margin softmax for face verification. In *IEEE Signal Processing Letters*, pages 926–930. IEEE, 2018. 4, 5, 6
- [47] Hao Wang, Yitong Wang, Zheng Zhou, Xing Ji, Dihong Gong, Jingchao Zhou, Zhifeng Li, and Wei Liu. Cosface: Large margin cosine loss for deep face recognition. In *Proceedings of the IEEE conference on computer vision and pattern recognition*, pages 5265–5274, 2018. 1, 2, 4, 5, 6, 7
- [48] Cameron Whitelam, Edward Taborsky, Austin Blanton, Brian Maze, Joshua Adams, Tim Miller, Nathan Kalka,

- Karthik Jain, J Ross Duncan, Kevin Allen, et al. Iarpa janus benchmark-b face dataset. In *Proceedings of the IEEE Conference on Computer Vision and Pattern Recognition Workshops (CVPRW)*, pages 90–98, 2017. 3
- [49] Lior Wolf, Tal Hassner, and Itay Maoz. Face recognition in unconstrained videos with matched background similarity. In *CVPR 2011*, pages 529–534. IEEE, 2011. 2, 3, 4, 5
- [50] Cihang Xie, Jianyu Wang, Zhishuai Zhang, Zhou Ren, and Alan Yuille. Mitigating adversarial effects through randomization. *arXiv preprint arXiv:1711.01991*, 2017. 2, 8, 5
- [51] W Xu. Feature squeezing: Detecting adversarial examples in deep neural networks. *arXiv preprint arXiv:1704.01155*, 2017. 2, 8, 5
- [52] Xiao Yang, Dingcheng Yang, Yinpeng Dong, Hang Su, Wenjian Yu, and Jun Zhu. Robfr: Benchmarking adversarial robustness on face recognition. *arXiv preprint arXiv:2007.04118*, 2020. 2, 3, 5, 8
- [53] Hongyang Zhang, Yaodong Yu, Jiantao Jiao, Eric Xing, Laurent El Ghaoui, and Michael Jordan. Theoretically principled trade-off between robustness and accuracy. In *International conference on machine learning*, pages 7472–7482. PMLR, 2019. 2, 8, 5
- [54] Kaipeng Zhang, Zhanpeng Zhang, Zhifeng Li, and Yu Qiao. Joint face detection and alignment using multitask cascaded convolutional networks. *IEEE signal processing letters*, 23(10):1499–1503, 2016. 5
- [55] Kaipeng Zhang, Ya-Liang Chang, and Winston Hsu. Deep disguised faces recognition. In *Proceedings of the IEEE Conference on Computer Vision and Pattern Recognition Workshops*, pages 32–36, 2018. 8
- [56] Ligang Zhang, Brijesh Verma, Dian Tjondronegoro, and Vinod Chandran. Facial expression analysis under partial occlusion: A survey. *ACM Computing Surveys (CSUR)*, 51(2):1–49, 2018. 2
- [57] Xiangyu Zhang, Xinyu Zhou, Mengxiao Lin, and Jian Sun. Shufflenet: An extremely efficient convolutional neural network for mobile devices. In *Proceedings of the IEEE Conference on Computer Vision and Pattern Recognition (CVPR)*, pages 6848–6856, 2018. 4, 5
- [58] Zhedong Zheng, Hao Tang, Ling Shao, Philip H.S. Torr, and Yi Zhang. Benchmarking robustness of 3d point cloud recognition against common corruptions. In *Proceedings of the IEEE/CVF Conference on Computer Vision and Pattern Recognition (CVPR)*, 2022. 3

OODFace: Benchmarking Robustness of Face Recognition under Common Corruptions and Appearance Variations

Supplementary Material

A. More Details of OOD Scenarios

A.1. Implementation Details of Corruptions

First, we describe the implementation details and hyperparameters of 20 common corruptions used in the LFW-C, CFP-C, and YTF-C benchmarks. Note that each corruption is evaluated at five severity levels, with specific hyperparameter configurations corresponding to each level.

Gaussian Noise. Gaussian noise simulates sensor noise by adding random values with a normal distribution to the image. The noise intensity is controlled by the standard deviation, with five levels of severity: {0.08, 0.12, 0.18, 0.26, 0.38}. Noise is added to each pixel, creating effects of varying intensities. We implement this using *imagecorruptions* [3] library, simulating different levels of Gaussian noise with predefined severities {1, 2, 3, 4, 5}.

Shot Noise. Shot noise simulates photon counting noise that occurs during image capture, particularly noticeable under low-light conditions. The intensity depends on the noise amplitude and the illumination level of the image. Severity levels are set as {60, 25, 12, 5, 3}, with higher levels introducing noticeable random brightness variations. We implement this using *imagecorruptions* [3] library, with severities {1, 2, 3, 4, 5}.

Impulse Noise. Impulse noise replaces random pixel values with extremes (e.g., 0 or 255) to simulate transmission errors in images. The intensity of the noise is determined by its density, with levels {0.03, 0.06, 0.09, 0.17, 0.27}. Higher noise density results in more black-and-white speckles. We implement this using *imagecorruptions* [3] library, with severities {1, 2, 3, 4, 5}.

Speckle Noise. Speckle noise simulates multiplicative noise caused by scattering, adding random values to each pixel. Noise intensity is controlled by levels {0.15, 0.2, 0.35, 0.45, 0.6}. As the intensity increases, the image becomes blurrier and the speckles more pronounced. We implement this using *imagecorruptions* [3] library, with severities {1, 2, 3, 4, 5}.

Defocus Blur. Defocus blur simulates the effect of mis-focused cameras, with the degree of blur controlled by the focal radius. Severity levels {1, 2, 3, 4, 5} correspond to different blur radii: level 1 uses a radius of 3, level 2 uses 4, level 3 uses 6, level 4 uses 8, and level 5 uses 10. Alias blur parameters range from 0.1 to 0.5 for each level. We implement this using *imagecorruptions* [3] library to simulate defocus blur with predefined severity levels.

Motion Blur. Motion blur simulates the relative move-

ment of the camera or object during image capture. The intensity is controlled by the blur radius and standard deviation, which represent the motion’s angle and length. Parameters for the five levels are: {radius: 10, std: 3}, {radius: 15, std: 5}, {radius: 15, std: 8}, {radius: 15, std: 12}, {radius: 20, std: 15}. Higher levels result in increased blur and more prominent directional effects. We implement this using *imagecorruptions* [3] library, using severities {1, 2, 3, 4, 5}.

Zoom Blur. Zoom blur simulates the effect of changing the camera focal length during capture, with intensity controlled by the zoom factor. The zoom factors for five severity levels are: {1.01, 1.11}, {1.01, 1.16}, {1.01, 1.21}, {1.01, 1.26}, {1.01, 1.31}. Higher severity levels produce stronger zoom effects. We implement this using *imagecorruptions* [3] library, simulating predefined severity levels.

Fog. Fog simulates the scattering effect caused by fog in the atmosphere, reducing image brightness and contrast. The intensity levels are set as {0.1, 0.2, 0.3, 0.4, 0.5}. As the intensity increases, the image becomes more blurred and grayish. Specifically, we implement this using *imagecorruptions* [3] library, and the fog effect is implemented by adjusting image brightness and applying intensity factors, with parameters set for each level as {1.5, 2}, {2.0, 2.0}, {2.5, 1.7}, {2.5, 1.5}, and {3.0, 1.4}. These parameters control the strength and diffusion of the fog effect.

Frost. Frost simulates the effect of frost forming on glass surfaces, with intensity controlled by frost density. The intensity levels are {0.1, 0.2, 0.3, 0.4, 0.5}, and as intensity increases, the image becomes increasingly obscured by frost, with details becoming blurred. We implement this using *imagecorruptions* [3] library, specific intensity factors are set as {1.0, 0.4}, {0.8, 0.6}, {0.7, 0.7}, {0.65, 0.7}, and {0.6, 0.75}, controlling the strength and coverage of the frost effect.

Snow. Snow simulates the appearance of snow by adding snowflake particles to the image, with intensity controlled by the density and size of the flakes. The intensity levels are {10, 20, 30, 40, 50}, we implement this using *imagecorruptions* [3] library, with specific parameters as {0.1, 0.3, 3, 0.5, 10, 4, 0.8}, {0.2, 0.3, 2, 0.5, 12, 4, 0.7}, {0.55, 0.3, 4, 0.9, 12, 8, 0.7}, {0.55, 0.3, 4.5, 0.85, 12, 8, 0.65}, and {0.55, 0.3, 2.5, 0.85, 12, 12, 0.55}. These parameters control snowflake size, density, blur, and coverage. As intensity increases, snow density rises, gradually obscuring image details.

Spatter. Spatter simulates the effect of splashes, such

as water or paint, on a surface. The intensity is controlled by the size and distribution of splash particles. The intensity levels are {1, 5, 10, 15, 20}, we implement this using *imagecorruptions* [3] library, with specific parameters as {0.65, 0.3, 4, 0.69, 0.6, 0}, {0.65, 0.3, 3, 0.68, 0.6, 0}, {0.65, 0.3, 2, 0.68, 0.5, 0}, {0.65, 0.3, 1, 0.65, 1.5, 1}, and {0.67, 0.4, 1, 0.65, 1.5, 1}. These parameters control the number, size, blur, and coverage of splashes. With higher intensity levels, splash marks become more prominent, with particles increasing and gradually covering image details.

Contrast. Contrast adjustment modifies the range of brightness and the difference between light and dark areas, affecting the visual appearance of the image. The contrast levels are {0.4, 0.3, 0.2, 0.1, 0.05}, where higher values increase contrast and lower values decrease it. When contrast is increased, the light and dark areas become more distinct. Conversely, reduced contrast makes details and differences less visible. We implement this using *imagecorruptions* [3] library.

Brightness. Brightness adjustment changes the overall luminance of the image. The brightness levels are {0.1, 0.2, 0.3, 0.4, 0.5}, where lower values darken the image, and higher values brighten it. Increased brightness makes details more visible, but over-brightening may result in detail loss.

Saturate. Saturation adjustment affects the intensity of colors in the image. The saturation levels are {0.3, 0.1, 2.0, 5.0, 20.0}, with higher values indicating stronger color saturation. When saturation increases, colors become more vivid, while lower saturation results in softer colors.

JPEG Compression. JPEG compression simulates the information loss that occurs during image compression. The compression levels are {25, 18, 15, 10, 7}, where smaller values correspond to higher compression ratios, resulting in greater loss of image details and more noticeable compression artifacts. As the compression level increases, the image quality degrades, and more compression artifacts appear.

Pixelate. The pixelate effect blurs image details by reducing the resolution, with the intensity controlled by the size of the pixel blocks. The pixelation levels are {0.6, 0.5, 0.4, 0.3, 0.25}, where smaller values correspond to larger pixel blocks and more loss of image detail. We implement this using *imagecorruptions* [3] library.

Facial Distortion. Facial distortion distorts the image by simulating elastic deformations on the object’s surface, with the intensity controlled by the magnitude of the deformation. The deformation levels are {0.05, 0.065, 0.085, 0.1, 0.12}, where larger values result in stronger deformations of the image edges and shapes.

Random Occlusion. Random occlusion simulates object occlusion by randomly generating elliptical occlusion regions within the image. The area of occlusion is con-

trolled by the level, which is {5%, 10%, 15%, 20%, 25%}. Higher levels correspond to larger occlusion regions, resulting in more covered details. Specifically, occlusion regions are generated by randomly selecting multiple locations in the image and drawing ellipses at those positions. The size and position of each occlusion are random, with the occlusion area being proportional to the level. By adjusting the number and size of the occlusion regions, image details are covered to varying degrees.

Salt and Pepper Noise. Salt and pepper noise simulates dirty spots in an image by randomly setting some pixel values to 0 or 255. The noise density levels are {0.01%, 0.05%, 0.1%, 0.2%, 0.5%}, with higher levels introducing more noise points in the image. Specifically, the intensity of the noise is controlled by the noise ratio at each level, where 0.01% corresponds to fewer noise points, and 0.5% corresponds to more. Based on the noise density, the code calculates the number of pixels to which noise should be added and sets these pixels’ values to 0 or 255 at random positions to generate varying degrees of salt and pepper noise.

Color Shift. Color shift simulates different lighting conditions or color changes by altering the hue values of the image. The hue shift levels are {0, 7, 14, 21, 28}, where each level represents the maximum hue shift in degrees (0-180). Higher levels result in more noticeable hue shifts and a more varied color palette. The magnitude of the hue shift is controlled by the level, followed by randomly generating a hue shift value within this range, applied to the image in the HSV color space, thereby altering the color style of the image.

A.2. Appearance Variations Implementation Details

Next, we present the implementation details and hyperparameters for the 10 appearance variations across the three benchmarks: LFW-V, CFP-V, and YTF-V. Additionally, each corruption has five severity levels.

Age-. Age reduction is an important factor in facial changes, as facial features undergo noticeable alterations with age, such as changes in skin texture, sagging, wrinkles, and overall facial structure. We simulate facial rejuvenation using a generative model, which reduces signs of aging, making the face appear younger. The age reduction levels consist of five stages, ranging from mild to significant rejuvenation. The higher the level, the more pronounced the reduction in aging signs. We implement this using the PTI [39] algorithm.

Age+. In contrast to age reduction, age increment simulates the process of facial aging, with features such as wrinkles, sagging, and skin aging becoming more prominent. We simulate facial aging using a generative model, increasing the aging features to make the face appear older. The age increment levels are also divided into five stages, with

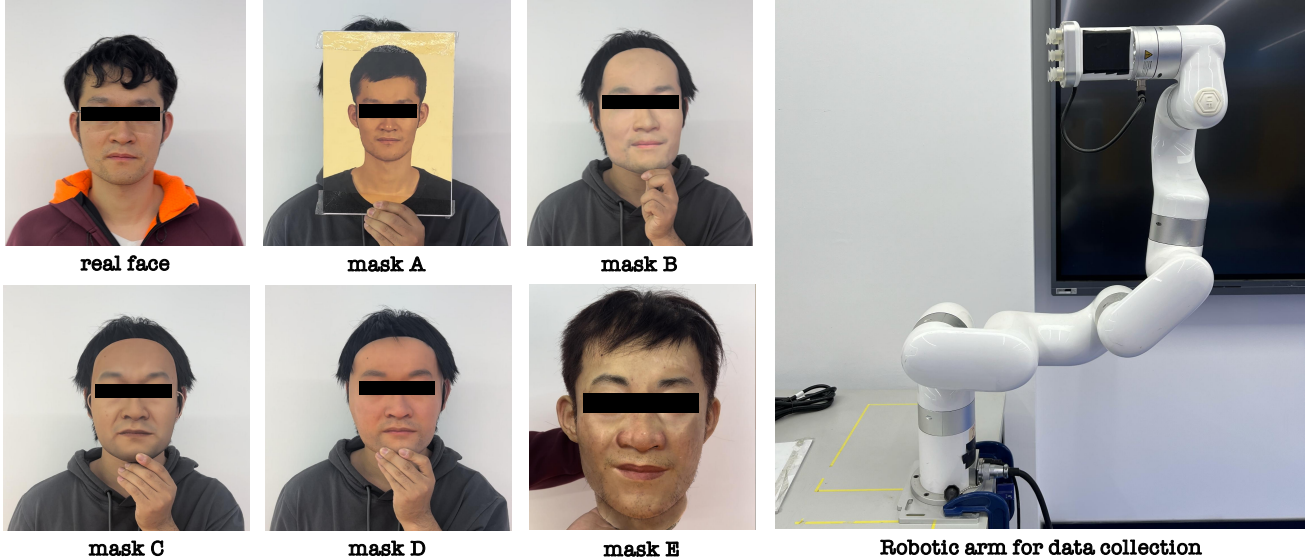


Figure A.1. Display of face masks and robotic arm for data collection

| Models | | Input Transformation | | | | Adversarial Training | | | | | |
|--------------------|-------------------|----------------------|------------|--------------|---------------|----------------------|---------------|------------|------------|-------|------------|
| Corruptions | | Softmax-BR | Softmax-RP | Softmax-JPEG | TradesSoftmax | TradesCosFace | TradesArcFace | PGDSoftmax | PGDCosFace | PGDAm | PGDArcFace |
| None (clean) | | 99.53 | 99.48 | 99.53 | 90.65 | 90.43 | 94.92 | 90.85 | 85.53 | 84.57 | 87.07 |
| Lighting & Weather | Brightness | 99.02 | 98.85 | 98.94 | 84.64 | 84.33 | 91.23 | 86.50 | 79.62 | 77.79 | 80.25 |
| | Contrast | 90.92 | 88.79 | 89.13 | 66.46 | 64.21 | 62.02 | 61.64 | 57.84 | 58.80 | 59.46 |
| | Saturate | 99.29 | 99.20 | 99.29 | 89.16 | 87.39 | 93.99 | 89.64 | 84.21 | 82.62 | 86.27 |
| | Fog | 89.89 | 89.12 | 89.72 | 61.22 | 59.05 | 59.14 | 57.67 | 55.95 | 57.42 | 56.44 |
| | Snow | 95.14 | 94.31 | 95.13 | 84.16 | 80.83 | 88.68 | 85.65 | 79.45 | 77.36 | 80.71 |
| Sensor | Defocus Blur | 87.11 | 86.78 | 87.38 | 83.90 | 70.14 | 80.44 | 83.41 | 77.41 | 78.30 | 79.61 |
| | Color Shift | 99.46 | 99.39 | 99.44 | 88.69 | 87.17 | 93.71 | 88.33 | 81.54 | 78.68 | 83.83 |
| | Pixelate | 98.91 | 98.81 | 98.91 | 89.72 | 88.41 | 93.96 | 90.04 | 84.28 | 83.86 | 86.10 |
| Movement | Motion Blur | 94.12 | 93.58 | 94.38 | 85.69 | 79.42 | 86.25 | 85.60 | 79.49 | 80.06 | 81.81 |
| | Zoom Blur | 99.06 | 98.93 | 99.05 | 89.60 | 88.50 | 93.72 | 90.27 | 84.30 | 83.86 | 86.32 |
| | Facial Distortion | 92.37 | 92.19 | 92.46 | 87.37 | 81.40 | 89.30 | 86.50 | 82.12 | 81.70 | 83.60 |
| Data & Processing | Gaussian Noise | 81.74 | 81.34 | 80.61 | 79.05 | 79.03 | 81.08 | 71.37 | 71.01 | 70.63 | 73.78 |
| | Impulse Noise | 83.63 | 83.11 | 82.39 | 75.65 | 78.89 | 79.05 | 72.05 | 70.06 | 69.79 | 73.26 |
| | Shot Noise | 78.61 | 78.16 | 77.54 | 76.34 | 76.00 | 76.79 | 68.23 | 68.48 | 67.86 | 71.09 |
| | Speckle Noise | 86.18 | 85.71 | 84.78 | 78.28 | 78.69 | 80.63 | 71.46 | 70.99 | 69.96 | 73.33 |
| | Salt Pepper Noise | 64.83 | 64.27 | 66.48 | 68.31 | 67.48 | 66.51 | 60.96 | 62.60 | 63.29 | 66.88 |
| | Jpeg Compression | 98.93 | 98.88 | 98.94 | 90.19 | 88.93 | 94.43 | 90.54 | 84.80 | 84.17 | 86.65 |
| Occlusion | Random Occlusion | 94.08 | 93.17 | 94.02 | 72.39 | 68.36 | 73.09 | 72.00 | 68.23 | 64.94 | 68.84 |
| | Frost | 93.62 | 93.09 | 93.40 | 76.59 | 75.20 | 85.34 | 78.24 | 71.54 | 70.25 | 72.24 |
| | Spatter | 96.87 | 96.48 | 96.63 | 83.84 | 79.02 | 86.58 | 81.85 | 78.68 | 77.31 | 79.45 |
| Average | | 91.19 | 90.71 | 90.93 | 80.56 | 78.12 | 82.80 | 78.60 | 74.63 | 73.93 | 76.50 |

Table A.1. Accuracy of 19 robust FR models on LFW-C, categorized into input transformation, adversarial training.

higher levels corresponding to more pronounced aging features. This is implemented using the PTI [39] algorithm.

Mouth-close. Mouth closure is a significant facial expression change, commonly occurring in calm or serious states. We simulate the effect of mouth closure using a generative model, which tightens the lips and hides any expression. The mouth closure levels range from minimal to complete closure. The higher the level, the more pronounced the mouth closure, from slight changes to fully closed lips. We implement this using the PTI [39] algorithm.

Mouth-open. Mouth opening is typically associated with changes in facial expression, such as smiling, surprise, or speaking. We simulate the effect of mouth opening using a generative model, separating the lips to display various expressions. The mouth opening levels are also divided into

five stages, with higher levels corresponding to larger openings, from slight to fully open. We implement this using the PTI [39].

Eye-close. Eye closure is often related to fatigue, drowsiness, or certain emotional states. We simulate the effect of eye closure using a generative model, completely closing the eyes and covering the eyeballs. The eye closure levels range from slight to complete closure. The higher the level, the more pronounced the eye closure, from barely closed to fully shut. We implement this using the Ganspace [18], which uses principal component analysis (PCA) in the latent or feature space to identify important directions and demonstrates that large amounts of interpretable control can be defined by progressively perturbing along these main directions.

Eye-open. Eye opening is generally associated with alertness, wakefulness, or certain expressions. We simulate the effect of eye opening using a generative model, fully opening the eyes to display various emotions or states. The eye opening levels are similarly divided into five stages, with higher levels corresponding to larger openings, from slightly open to fully open. We implement this using the Ganspace [18].

Rotation-left. Left rotation of the face simulates different head poses, especially from side views. We simulate the effect of rotating the head to the left using an editing algorithm, enabling the face to change from different angles, thus enhancing the model’s adaptability to various viewpoints. The rotation levels are divided into five stages, with higher levels corresponding to larger angles, from slight leftward tilts to a full left-side view. We implement this using the PTI [39].

Rotation-right. Right rotation, in contrast to left rotation, simulates the effect of turning the face to the right. By adjusting the head rotation with an editing algorithm, we simulate the transition from a frontal view to a right-side perspective. The rotation levels are similarly divided into five stages, with higher levels corresponding to larger angles, from slight rightward tilts to a full right-side view. We implement this using the PTI [39].

Bangs & Glasses. Bangs and glasses are common facial occlusions that significantly alter the visual appearance of the face. By adding various accessories such as bangs or glasses (e.g., clear lenses, reflective lenses), we simulate real-life facial occlusion scenarios. The levels consist of five stages: wearing only clear-lens glasses, wearing only bangs, wearing reflective-lens glasses, wearing clear-lens glasses + bangs, and wearing reflective-lens glasses + bangs. Each level adds a different degree of facial occlusion, making facial features less visible. We implement this using the HiSD [26].

Makeup. Makeup can significantly alter the appearance of the face by changing features such as eyebrows, eyeliner, blush, and lipstick. We simulate different styles of makeup using a generative model Beautygan [25] to mimic real-life makeup scenarios. The makeup levels are divided into five stages, including: Japanese style, Korean style, and others.

B. Additional Results on LFW-C/V

Due to space limitations in the main text, we supplement additional data from LFW-C/V in this section.

B.1. LFW-C

For LFW-C, we design 5 levels for each corruption, ranging from level 1 (mild) to level 5 (extreme). In this section, we provide the specific data tables corresponding to levels 1-5, as shown in Tab. H.1, Tab. H.2, Tab. H.3, Tab. H.4, Tab. H.5. For each model, we present a radar chart that shows the

performance of the model across 20 different types of corruption, providing a clearer view of how the model’s performance varies under different types of corruption in each category, as shown in Fig. H.1. For each corruption category, we also provide line charts showing the model’s performance across the 5 levels of each corruption, illustrating the performance fluctuations as the level of corruption increases, as shown in Fig. H.3.

From the graded data results, we observe that as the severity level increases, the best-performing model against corruption changes. Taking “Open-source Model Eval” as an example, although AdaFace maintains the best average accuracy across all 5 levels, we find that at level 5, ArcFace significantly surpasses AdaFace in accuracy on Data & Processing. This further demonstrates that different models exhibit varying robustness to different types of corruption.

B.2. LFW-V

Similarly, for LFW-V, we design 5 levels for each variation. We supplement the specific data tables corresponding to levels 1-5 in this section, as shown in Tab. H.6, Tab. H.7, Tab. H.8, Tab. H.9, Tab. H.10. We present the radar charts in Fig. H.2, as well as the line charts showing the 5 levels for each category, in Fig. H.4.

C. Results on CFP-C/V

For CFP, we follow the experimental setup used for LFW-C/V and test 19 FR models on 20 types of common corruptions and 10 types of appearance variations, categorized into *Open-source Model Eval*, *Architecture Eval*, and *Loss Function Eval*. The test results are shown in Tab. H.11 and Tab. H.17. We also report the *Relative Corruption Error (RCE)*, as shown in Fig. H.5, for each model across different corruption categories. Additionally, in Appearance Variations, we further illustrate the *Relative Variation Error (RVE)*, as shown in Fig. H.6, for each model across variation categories.

We also provide the specific data tables corresponding to levels 1-5, as shown in Tab. H.12, Tab. H.13, Tab. H.14, Tab. H.15, Tab. H.16 and Tab. H.18, Tab. H.19, Tab. H.20, Tab. H.21, Tab. H.22. We present the radar charts and line charts showing the 5 levels for each category, in Fig. H.7, Fig. H.8 and Fig. H.9, Fig. H.10.

From the data, we observe that due to differences in data formats, the results on CFP-C/V show patterns that differ from those on LFW-C/V. Taking common corruptions as an example, overall, AdaFace still maintains the best robustness. However, at CFP-C level 1, we find that ElasticFace achieves the best results across all categories. This is because ElasticFace has a higher clean accuracy, and level 1 corruptions are relatively mild. From levels 2-5, AdaFace’s robustness gradually becomes more apparent. On CFP-V, ElasticFace, due to its higher clean accuracy, maintains the

highest accuracy across levels 1-5, which aligns with our conclusion in the main text that clean accuracy has a significant impact on variations.

D. Results on YTF-C/V

For YTF, we also provide the average accuracy data on YTF-C and YTF-V, shown in Tab. H.23 and Tab. H.29, respectively. We similarly report the *Relative Corruption Error (RCE)*, as shown in Fig. H.11, and the *Relative Variation Error (RVE)*, as shown in Fig. H.12. Additionally, we provide the specific data tables corresponding to levels 1-5, as shown in Tab. H.24, Tab. H.25, Tab. H.26, Tab. H.27, Tab. H.28 and Tab. H.30, Tab. H.31, Tab. H.32, Tab. H.33, Tab. H.34. Furthermore, we present the radar charts and line charts showing the 5 levels for each category, in Fig. H.13, Fig. H.14 and Fig. H.15, Fig. H.16.

For the YTF data, our findings are as follows: First, the FR models' clean accuracy on YTF is lower than on LFW and CFP. This is because YTF contains more complex data from various scenes, which is reflected in the final results. As shown in Tab. H.23, unlike LFW-C and CFP-C, the differences between models on YTF-C are more pronounced. For example, ArcFace achieves the highest clean accuracy and robustness in the Data & Processing category, while TransFace demonstrates advantages in specific categories like Snow, Color Shift, and Motion Blur.

On YTF-V, due to YTF's complex scenes, the performance drop caused by appearance variations is more severe, especially for ArcFace and ElasticFace. Although they achieve higher clean accuracy, their performance suffers more under variations. On the other hand, AdaFace, despite not having the highest clean accuracy, maintains the best robust accuracy under appearance variations. This finding slightly differs from the conclusions drawn on LFW and CFP.

E. Additional Results on Face Masks

In the field of face recognition (FR), masks typically refer to physical disguises used to deceive or conceal the identity of the wearer, preventing accurate recognition by the system. As an extension, we conduct physical experiments with masks.

In our experiments, we create five different types of masks using various collection methods and fabrication processes. We categorize them from *A* to *E* based on their realism, with *Mask A* being directly collected through photography and created using 2D printing technology with paper material. *Masks B* and *Masks C* are created by scanning facial data using 3D scanning technology, with sandstone and paper pulp materials, respectively. *Masks D* and *Masks E* are also created using 3D scanning and silicone material, with *Masks D* and *Masks E* having higher facial fit and elas-

ticity.

Then, we have another person wear the masks and conduct data collection using a robotic arm, as shown in Fig. A.1. The collected video data is captured from certain angles. We then extract video frames, associate them with the corresponding mask IDs as positive examples, and pair them with the person wearing the mask as negative examples to generate test data.

Subsequently, we test these masks on the Common Corruptions and Appearance Variations we design, in order to examine the characteristics of different masks and their impact in OOD scenarios. The results are shown in Tab. H.35, Tab. H.36, Tab. H.37, Tab. H.38, Tab. H.39 and Tab. H.40, Tab. H.41, Tab. H.42, Tab. H.43, Tab. H.44,. The data reveals differences from real faces and exhibits performance degradation trends that differ from those of real faces.

F. Data Augmentation as Potential Defense

We further explore potential defense measures to enhance robustness. Based on the methods described in [52], we employ existing defense strategies available, which can be categorized into two main approaches: *input transformation* (e.g., R&P [50], Bit-Red [51], JPEG [13]) and *adversarial training* (e.g., PGD-AT [32], TRADES [53]). We test 10 robust models based on these approaches, as shown in Tab. A.1. However, as we observe, for input transformation methods, there is no significant impact on the model's performance. Specifically, Bit-Red [51] increases the average accuracy of Softmax-IR by 0.02, while Bit-Red [51] and JPEG [13] result in slight performance degradation. For PGD-AT [32] and TRADES [53], which are designed for adversarial training, no gains are observed under natural corruptions during testing. On the contrary, due to a notable drop in clean data performance after adversarial training, the overall model performance declines. This indicates that existing defense strategies fail to address Out-of-Distribution (OOD) scenarios, and enhancing the robustness of FR remains an open challenge for future research.

G. VLMs as Potential solutions

In Sec.5.4 of the main text, we mentioned that, to explore better solutions for OOD scenarios in face recognition (FR), we investigated the use of Vision-Language Models (VLMs), a previously unexplored approach. The GPT-4o-mini we tested demonstrated strong FR capabilities, even being able to recognize specific types of corruptions present in images. We provide more examples, as shown in Fig D.1. When testing 50 pairs of faces with added common corruptions on the web version of GPT-4o-mini, all 50 pairs were successfully recognized, indicating the potential of VLMs in addressing the OOD data challenge.

In fact, we attempted to use the GPT API for batch

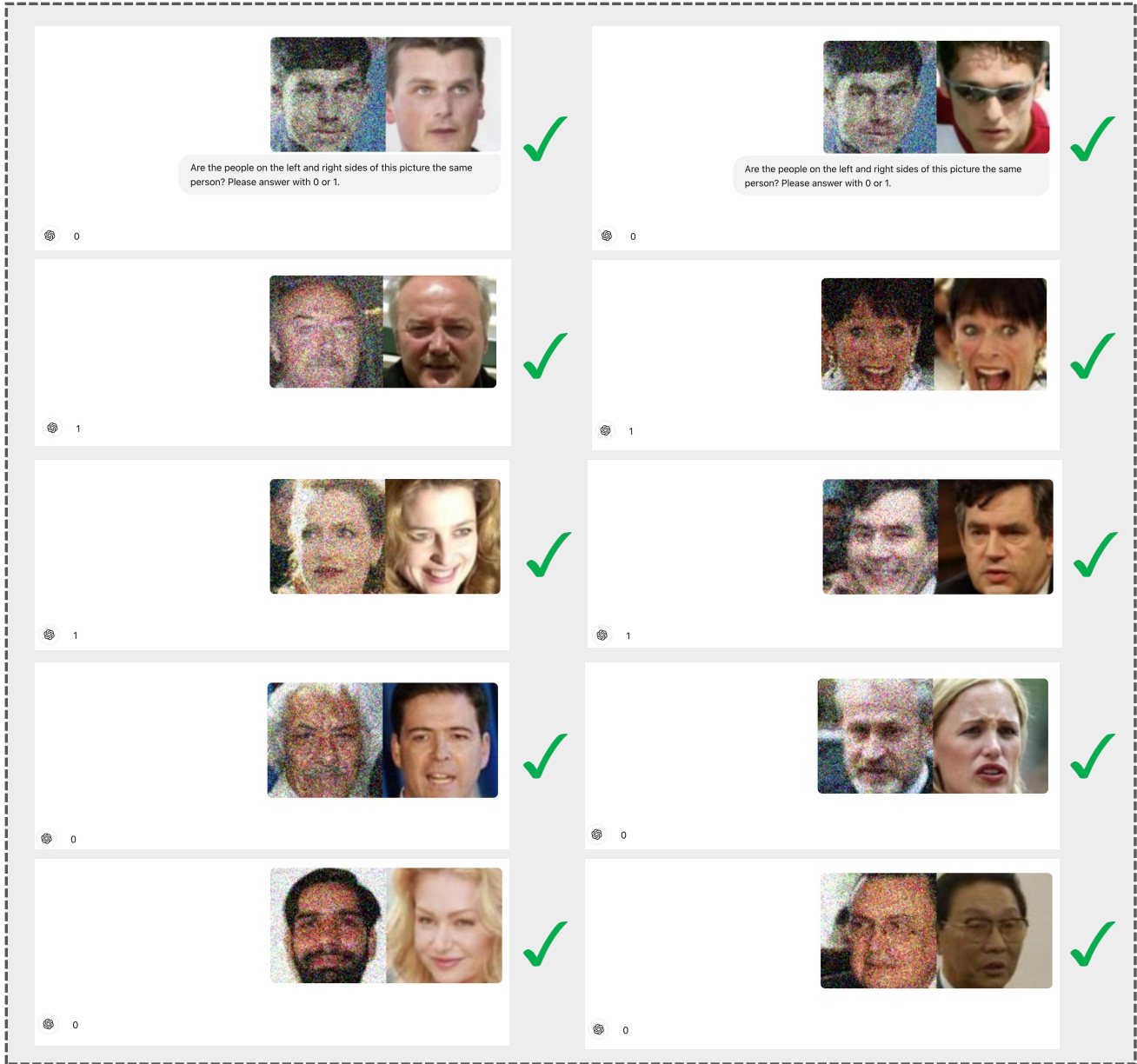


Figure D.1. Additional results on testing GPT-4 mini for FR.

testing of face data, such as LFW. Unfortunately, the API version of GPT-4o-mini refuse to respond to face-related queries, stating that it “*Cannot perform face recognition tasks.*” This may be due to privacy concerns related to tasks involving FR, which are considered sensitive and subject to security alignment policies, leading to the refusal. In our experiments, we also test models such as Claude 3 Sonnet and Gemini, but they do not seem to return correct FR results. Therefore, while the results with GPT-4o-mini suggest that leveraging the generalization capabilities of large models may be a promising solution for handling OOD scenarios,

the specific implementation details and usage methods still require further exploration.

H. More Visualization Results

To thoroughly assess the robustness of FR systems, in Sec.3.1, we follow [20] to define five severity levels for each type of corruption, with the common corruptions categorized into five levels ranging from level 1 (mild) to level 5 (extreme). In Sec.3.2, we define five severity levels for appearance variations, with each level representing an increase in perceived appearance interference. In this sec-

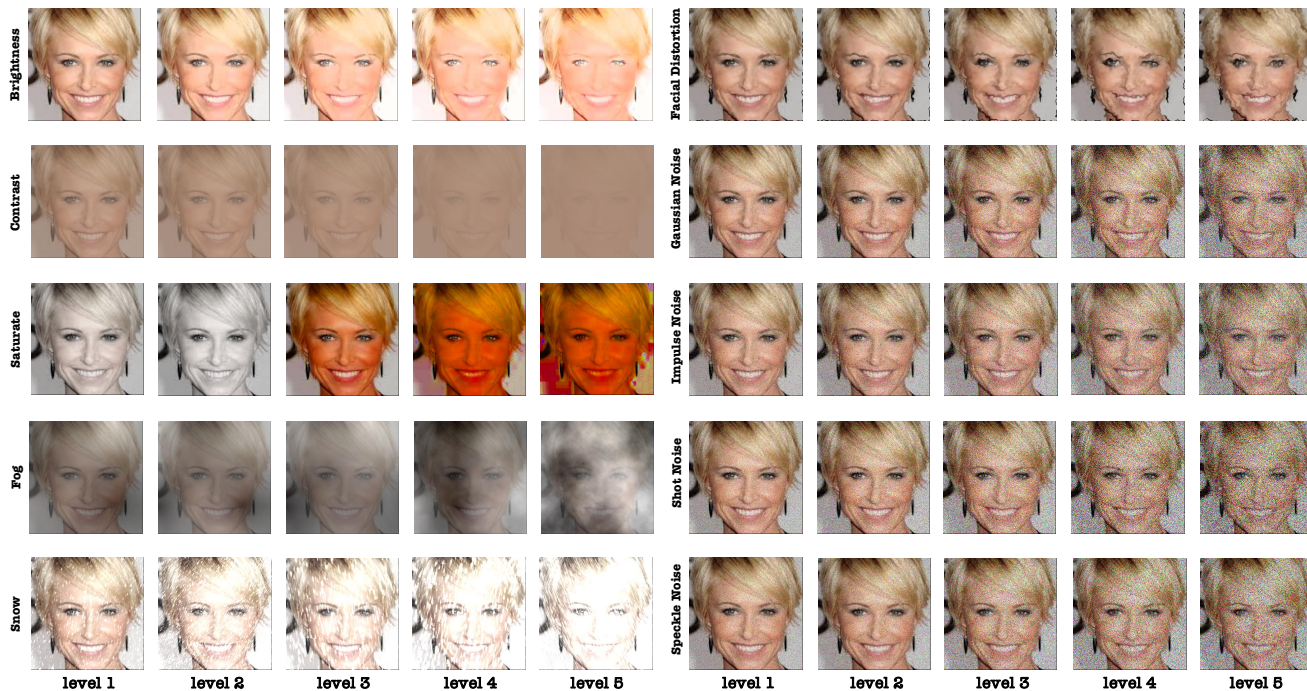


Figure D.2. Full visualization of common corruptions severity levels (part 1).

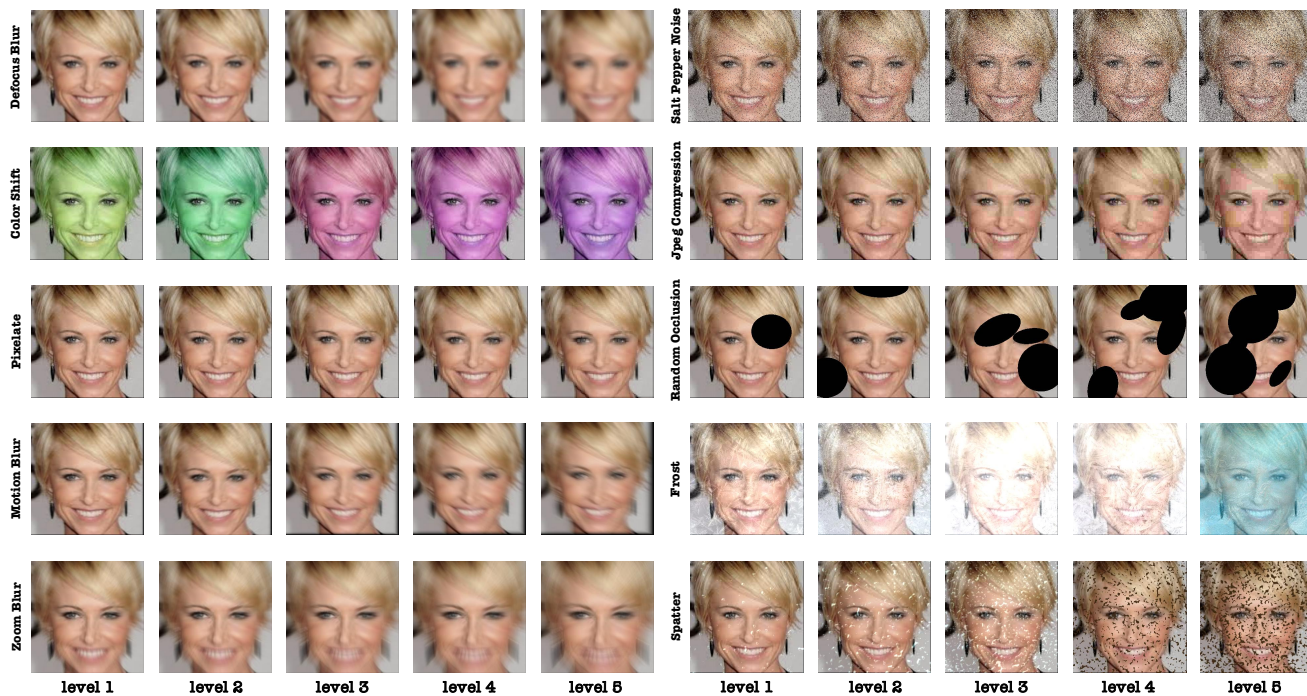


Figure D.3. Full visualization of common corruptions severity levels (part 2).

tion, we present the visualization results for all categories at severity levels 1 to 5, including 20 types of common corruptions as shown in Fig. D.2, Fig. D.3, and 10 types of appearance variations as shown in Fig. D.4.



Figure D.4. Full visualization of appearance variations severity levels.

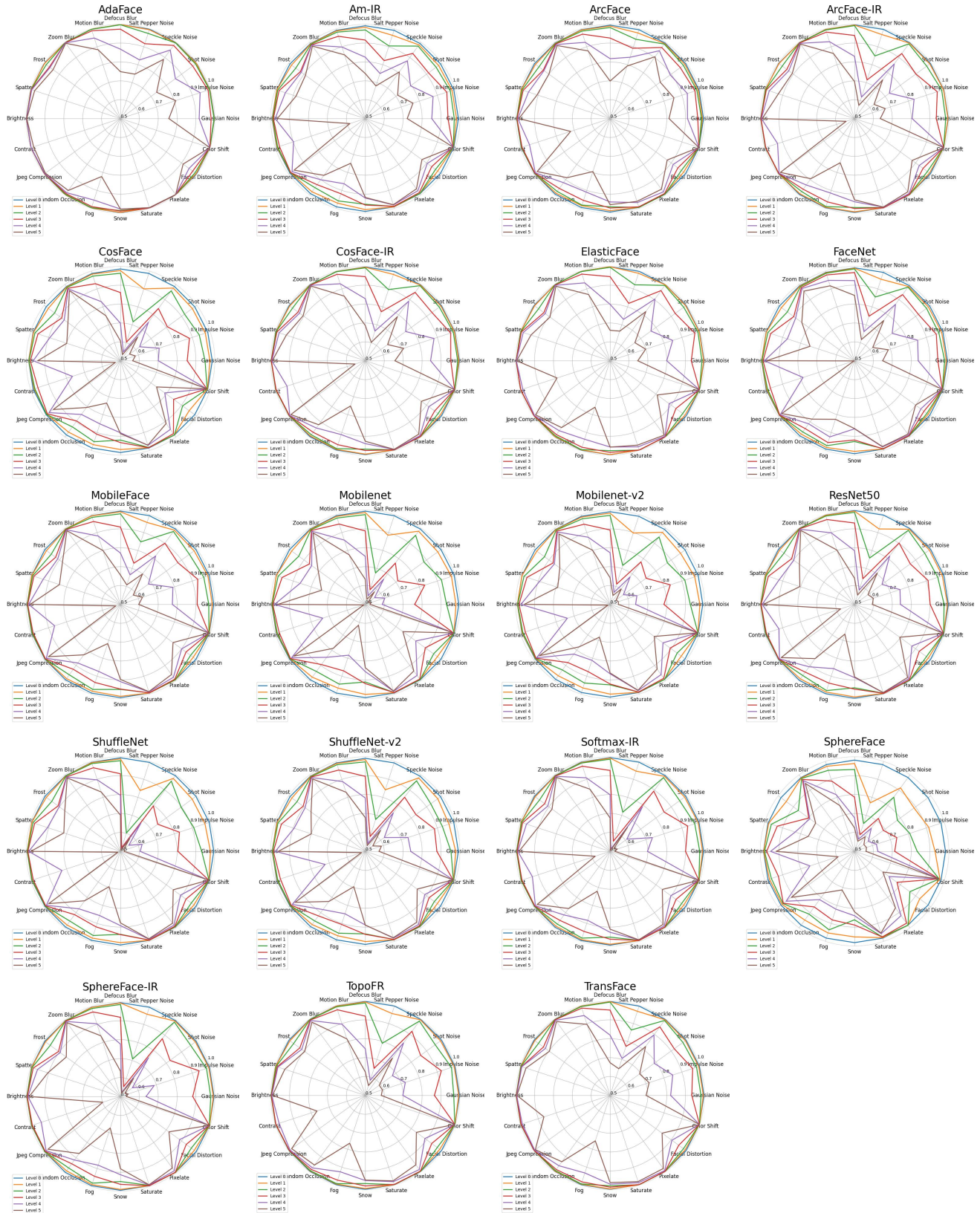


Figure H.1. Graded radar charts for each model on LFW-C.

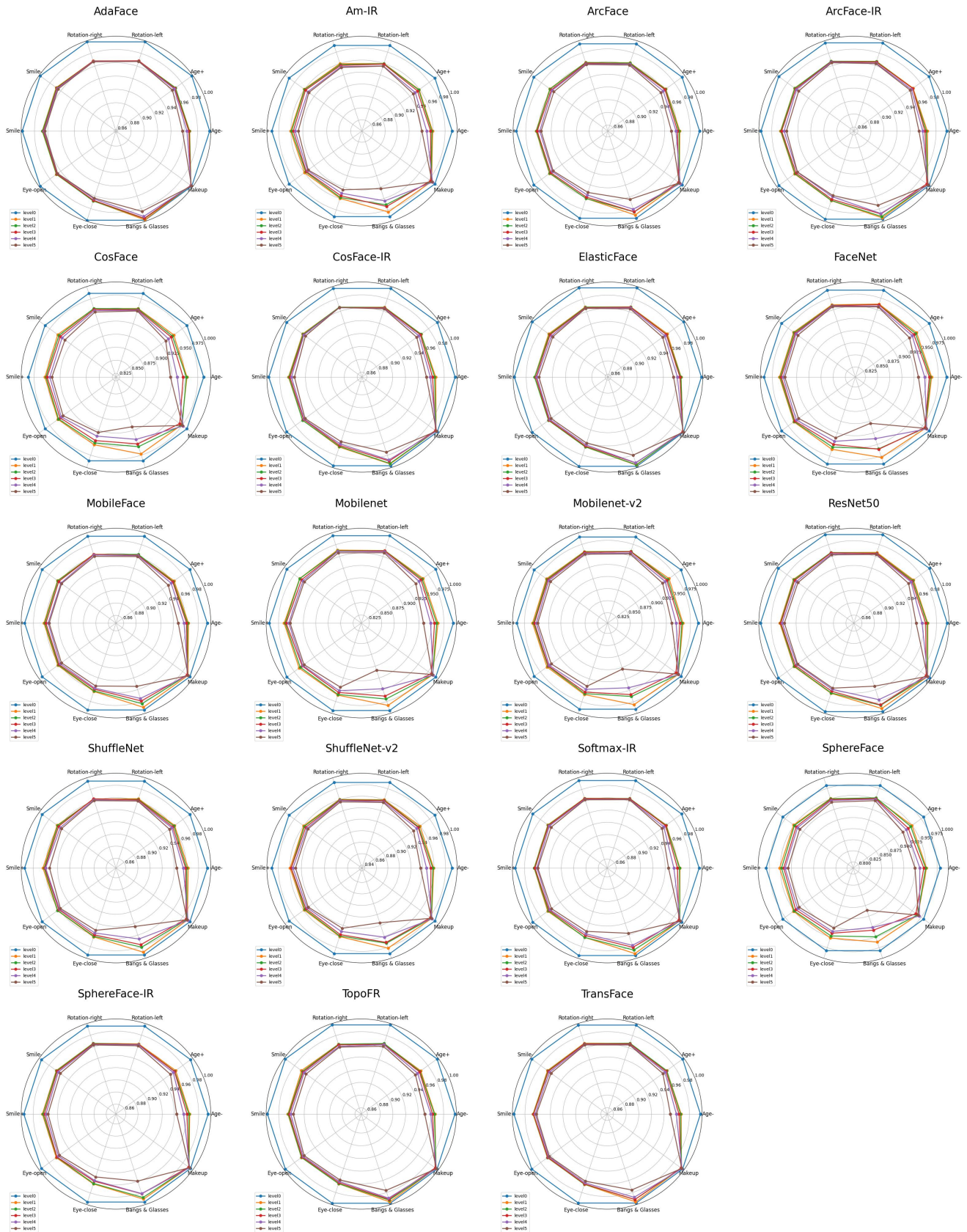


Figure H.2. Graded radar charts for each model on LFW-V.

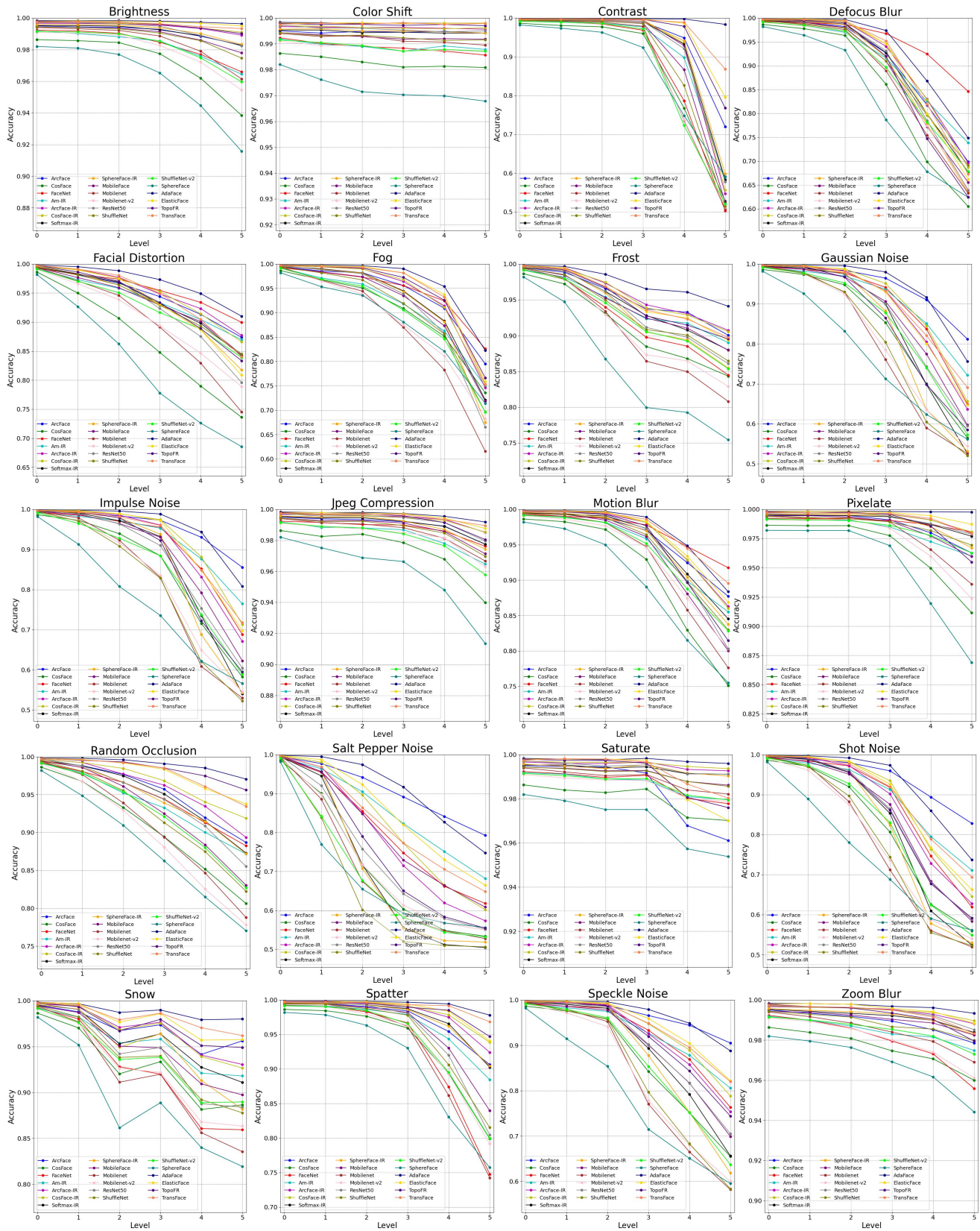


Figure H.3. Graded line charts for each corruption on LFW-C.

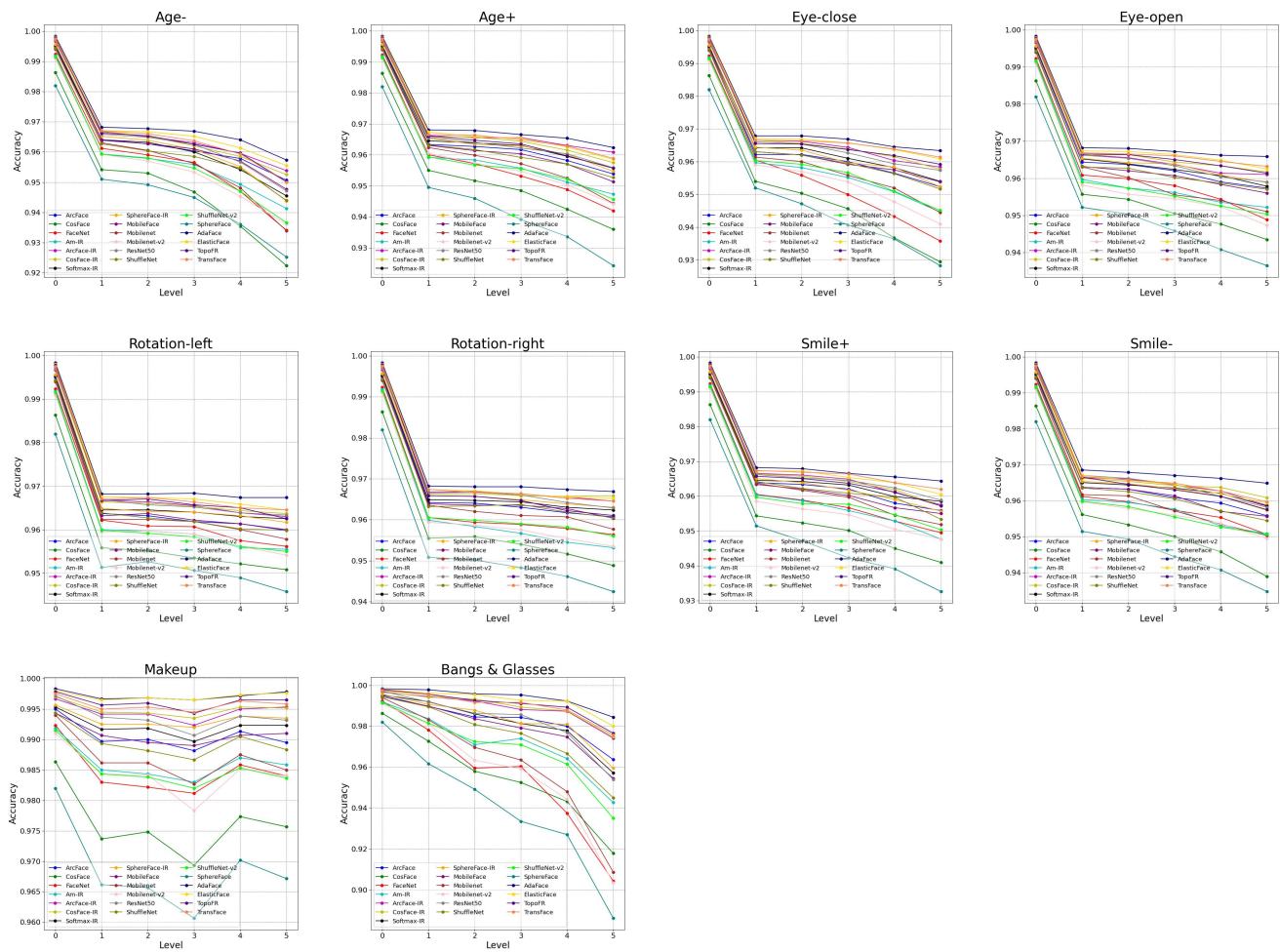


Figure H.4. Graded line charts for each corruption on LFW-V.

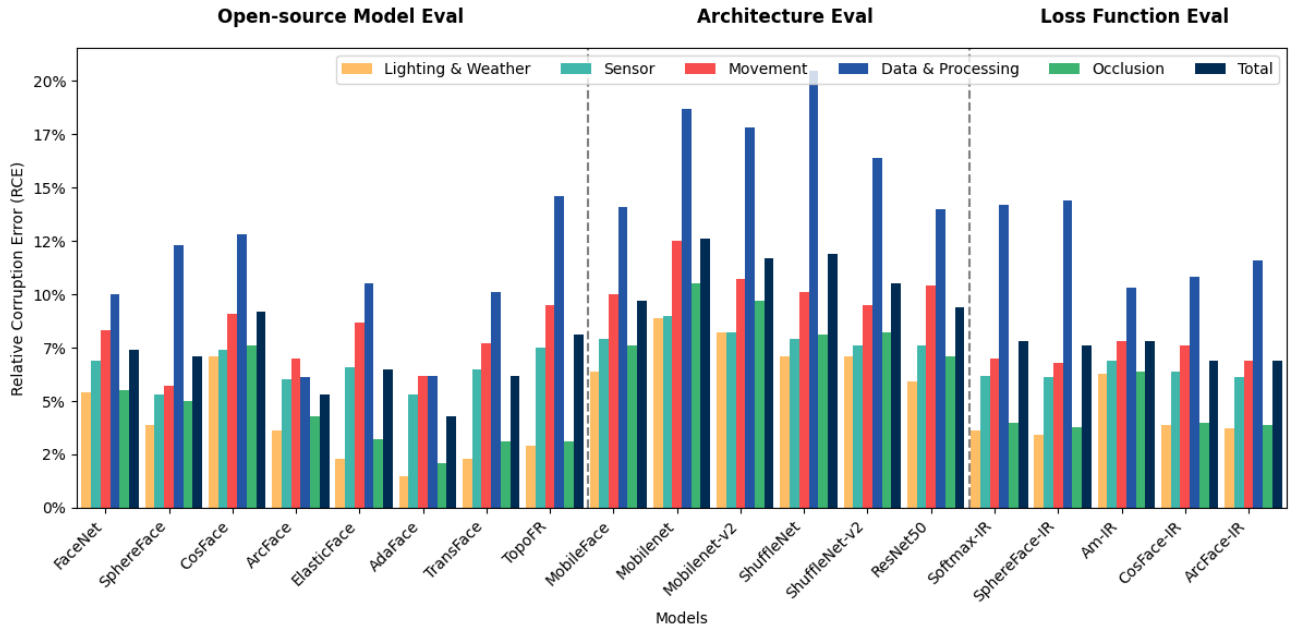


Figure H.5. RCE results on CFP-C.

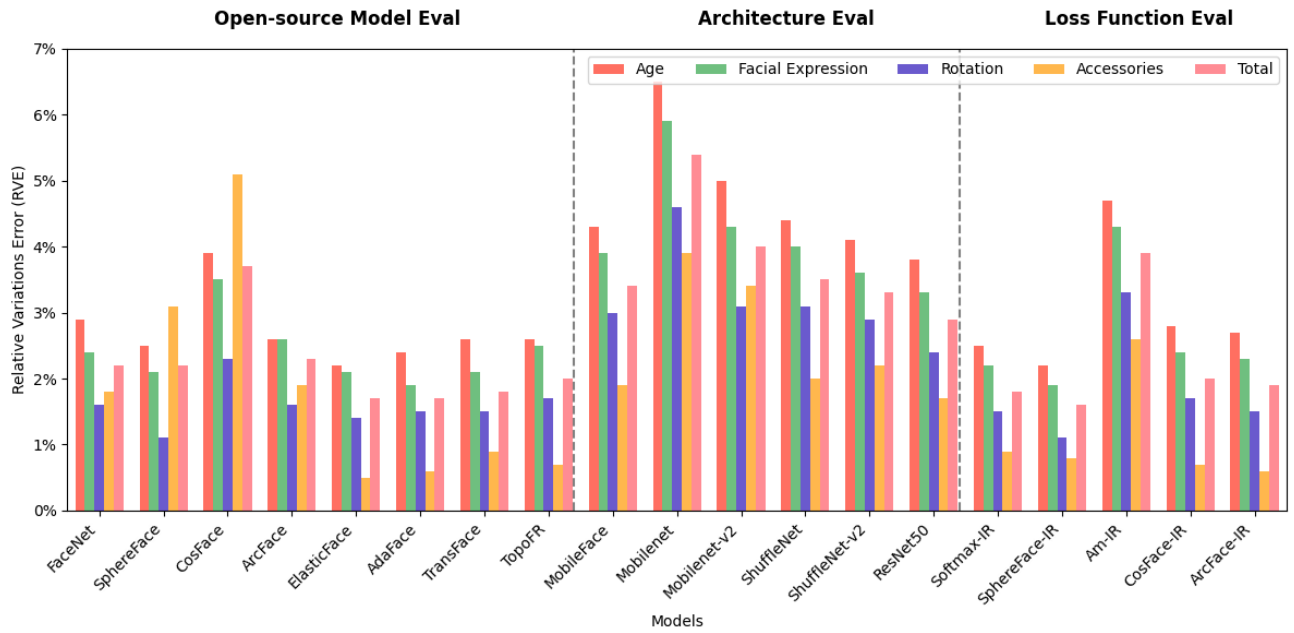


Figure H.6. RVE results on CFP-V.

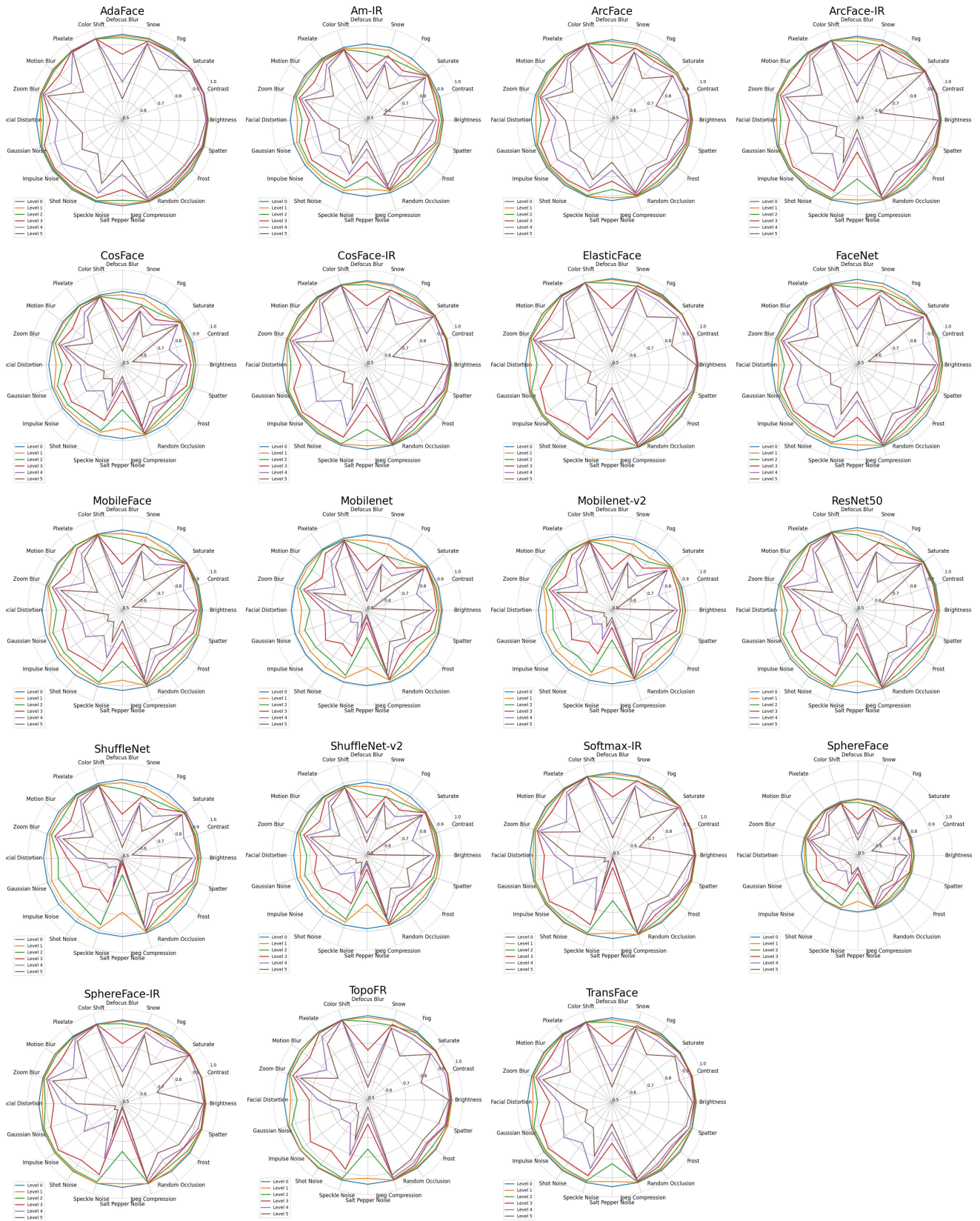


Figure H.7. Graded radar charts for each model on CFP-C.

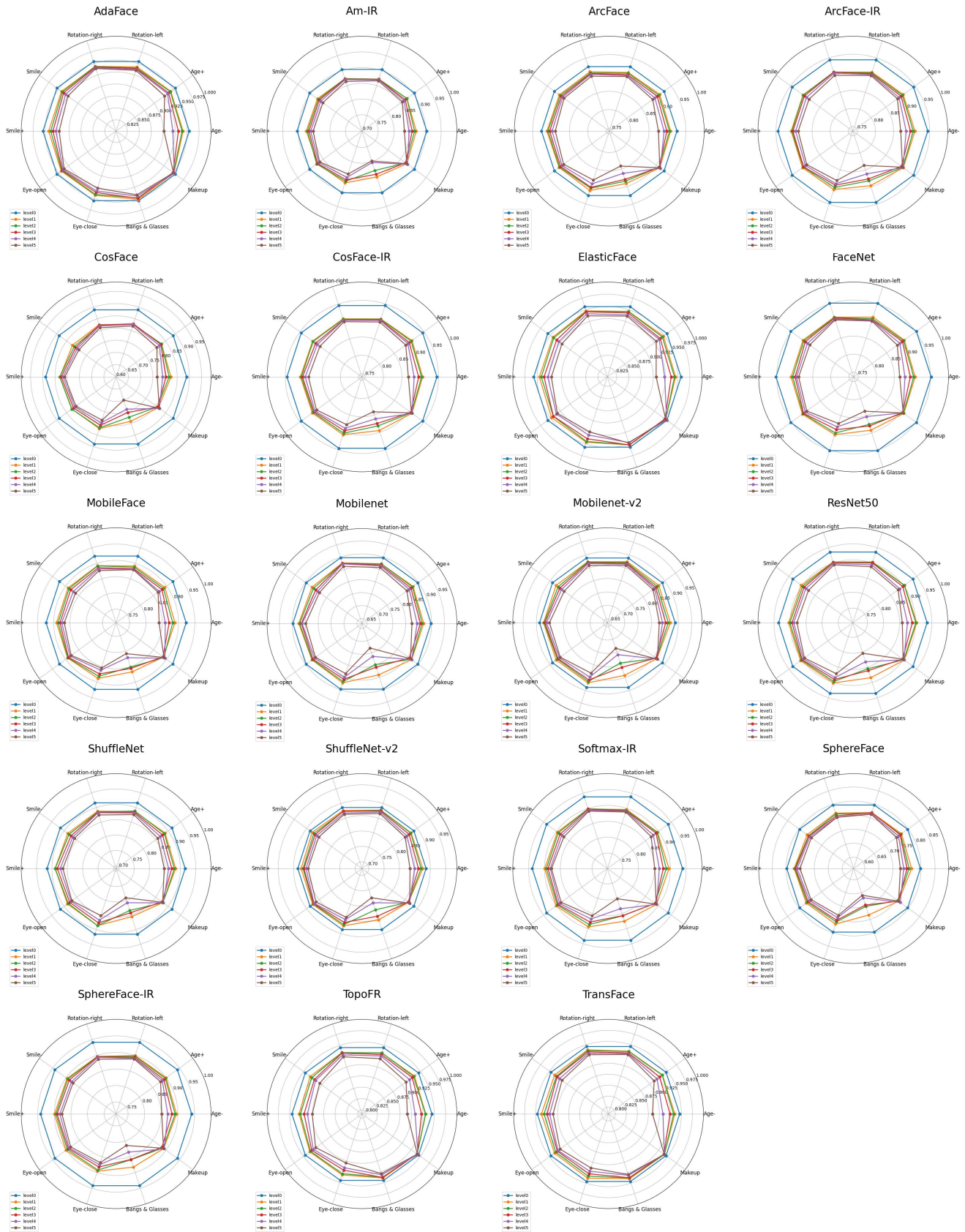


Figure H.8. Graded radar charts for each model on CFP-V.

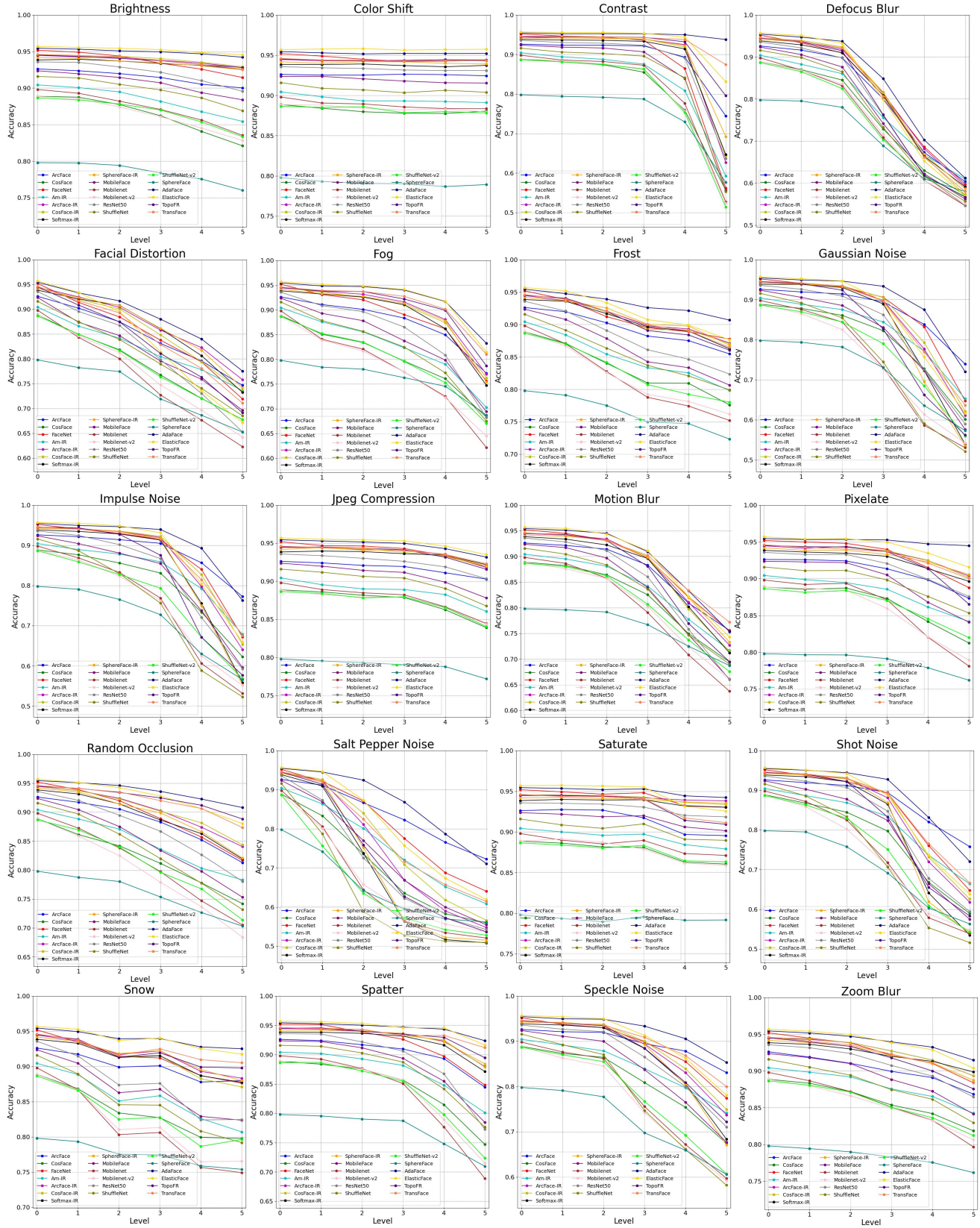


Figure H.9. Graded line charts for each corruption on CFP-C.

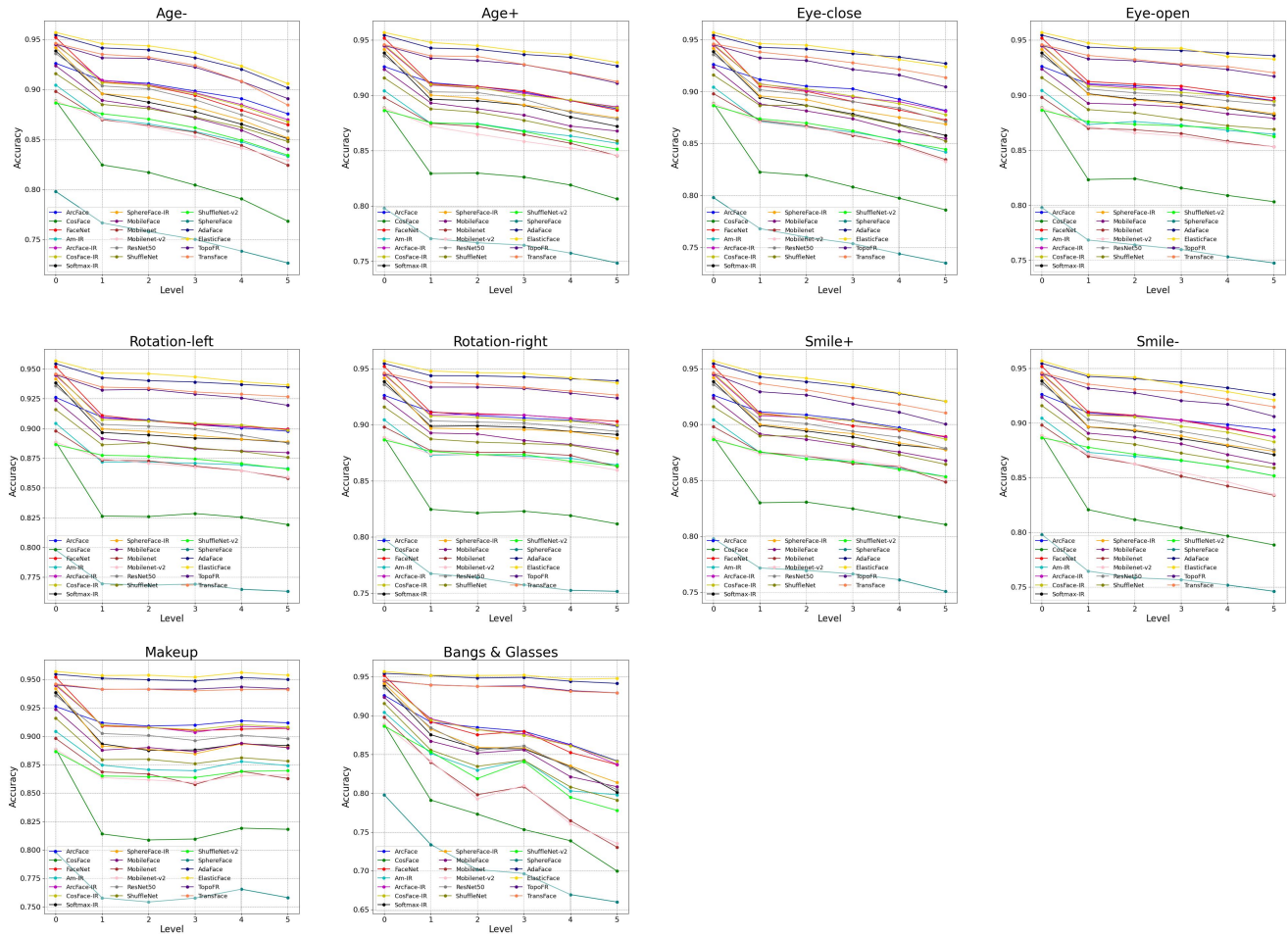


Figure H.10. Graded line charts for each corruption on CFP-V.

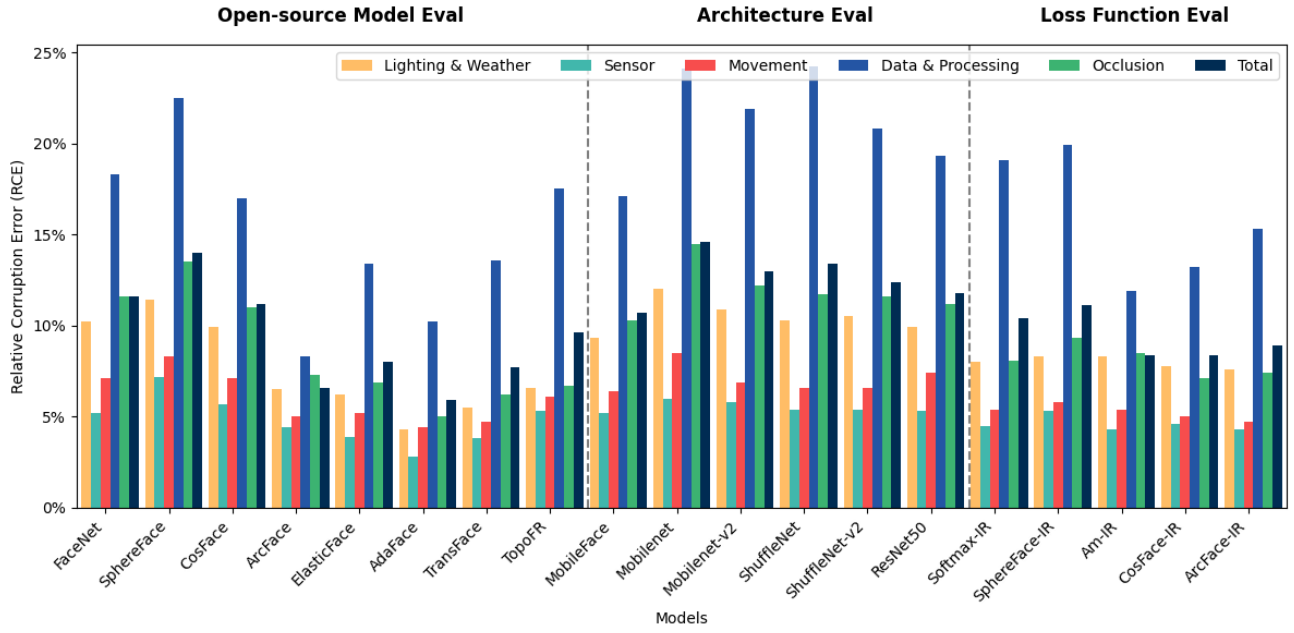


Figure H.11. RCE results on YTF-C.

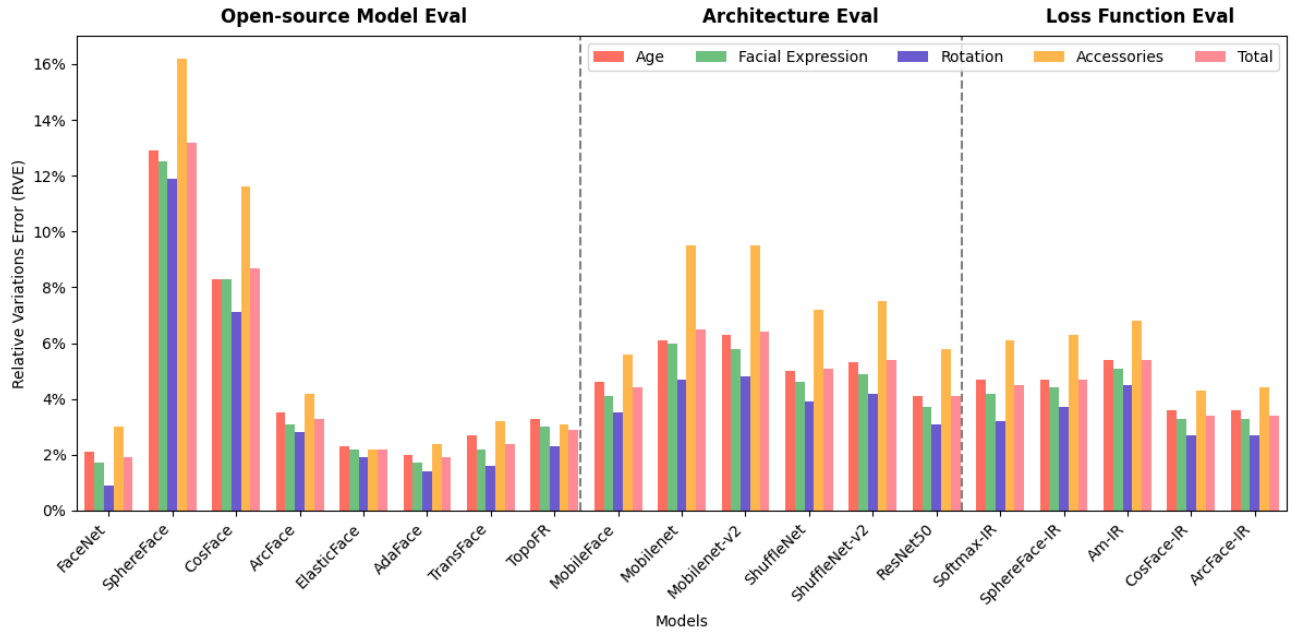


Figure H.12. RVE results on YTF-V.

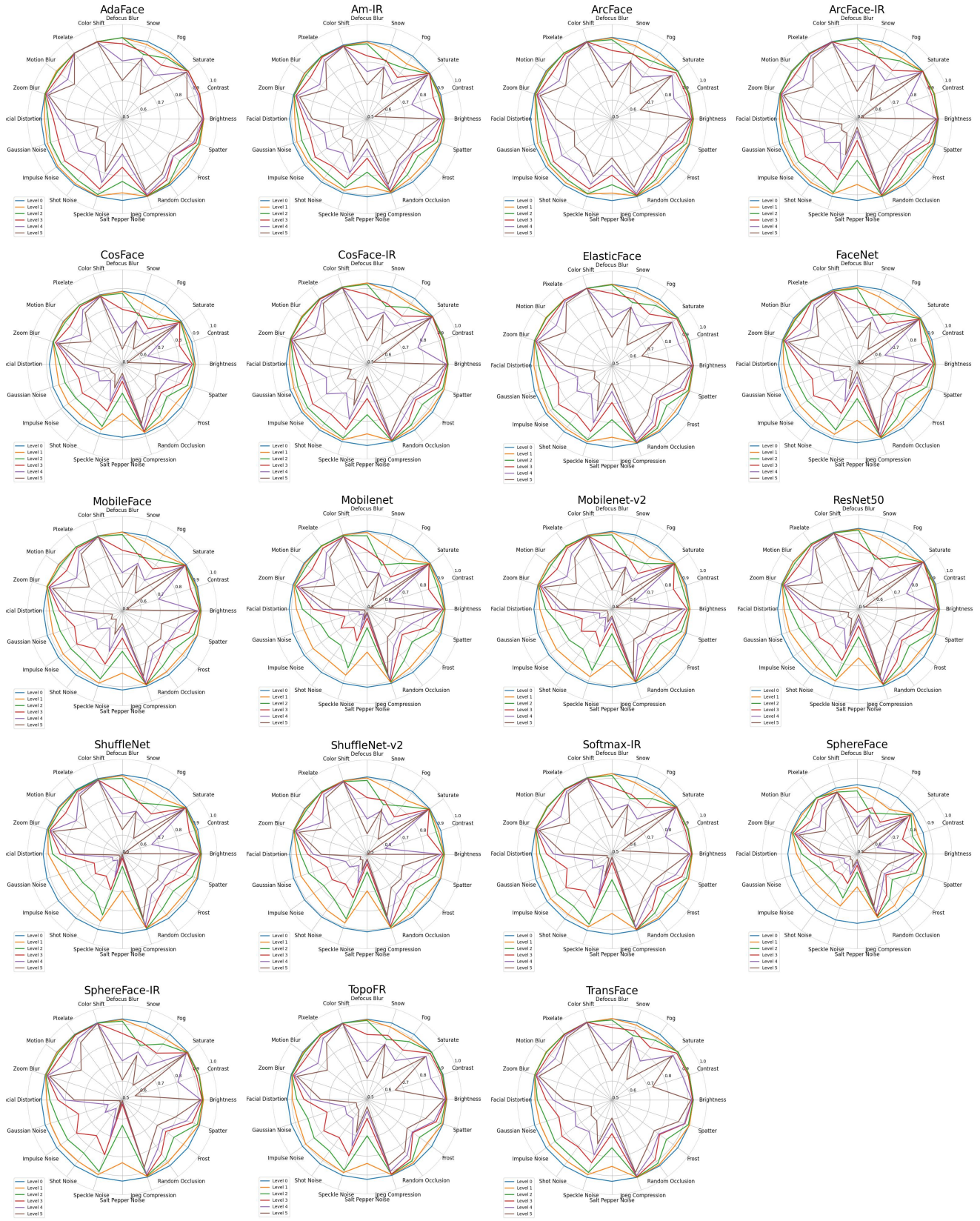


Figure H.13. Graded radar charts for each model on YTF-C.

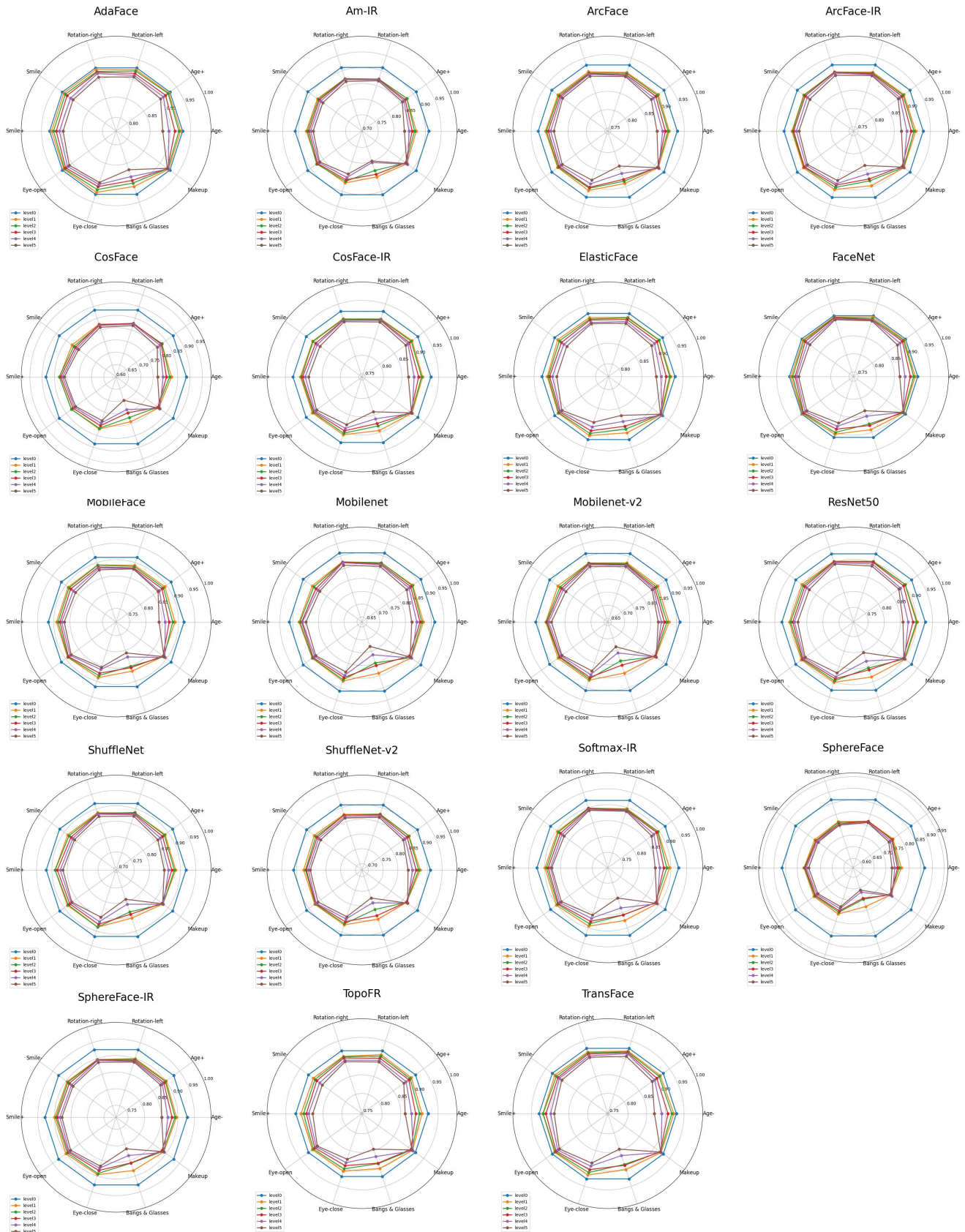


Figure H.14. Graded radar charts for each model on YTF-V.

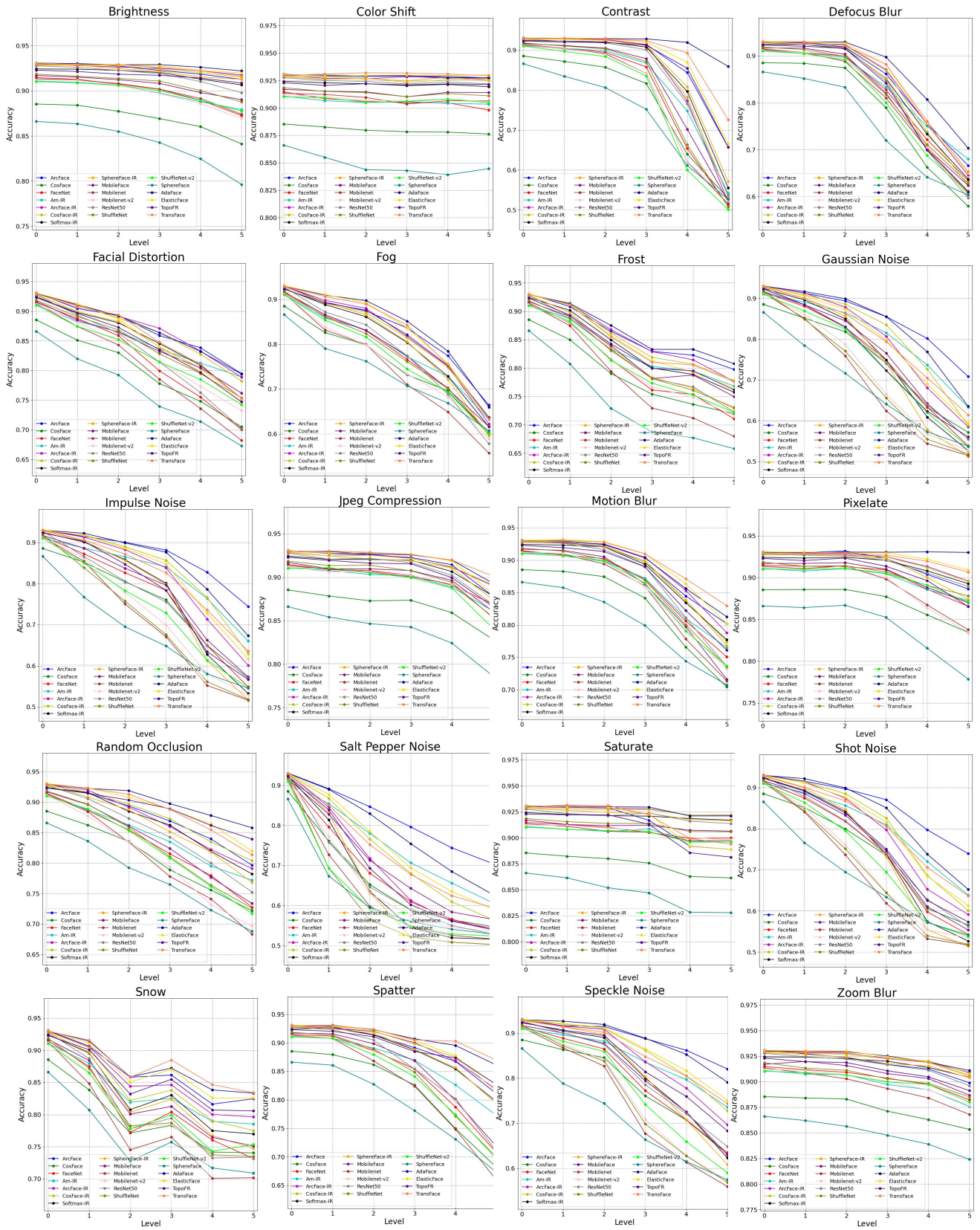


Figure H.15. Graded line charts for each corruption on YTF-C.

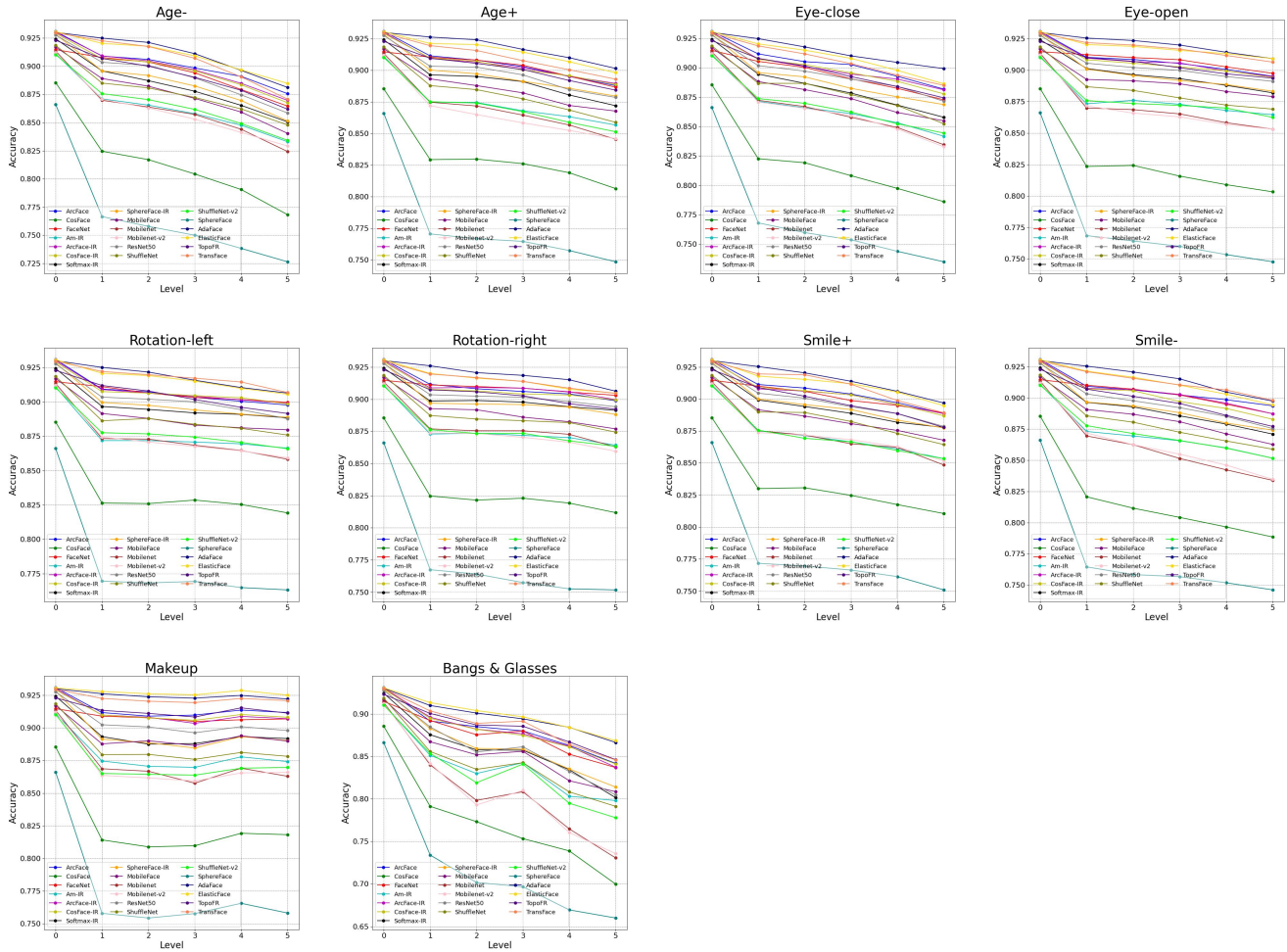


Figure H.16. Graded line charts for each corruption on YTF-V.

| Models | | Mask-B | | | | | | | |
|--------------------|-------------------|---------|------------|---------|---------|-------------|---------|-----------|--------|
| Corruptions | | FaceNet | SphereFace | CosFace | ArcFace | ElasticFace | AdaFace | TransFace | TopoFR |
| None (clean) | | 100.00 | 100.00 | 100.00 | 100.00 | 100.00 | 100.00 | 100.00 | 100.00 |
| Lighting & Weather | Brightness | 100.00 | 100.00 | 100.00 | 100.00 | 100.00 | 100.00 | 100.00 | 100.00 |
| | Contrast | 93.21 | 100.00 | 89.72 | 88.81 | 90.00 | 100.00 | 98.90 | 100.00 |
| | Saturate | 100.00 | 100.00 | 100.00 | 100.00 | 100.00 | 100.00 | 100.00 | 100.00 |
| | Fog | 76.51 | 87.80 | 70.92 | 90.55 | 91.38 | 95.87 | 94.40 | 94.68 |
| | Snow | 90.18 | 94.95 | 88.17 | 99.91 | 98.35 | 99.91 | 96.88 | 99.63 |
| Sensor | Defocus Blur | 89.08 | 88.81 | 70.55 | 80.00 | 80.00 | 100.00 | 98.53 | 100.00 |
| | Color Shift | 100.00 | 100.00 | 100.00 | 100.00 | 100.00 | 100.00 | 100.00 | 100.00 |
| | Pixelate | 100.00 | 100.00 | 99.91 | 100.00 | 100.00 | 100.00 | 100.00 | 100.00 |
| Movement | Motion Blur | 95.78 | 94.68 | 86.24 | 92.20 | 94.22 | 99.17 | 99.45 | 99.91 |
| | Zoom Blur | 97.25 | 100.00 | 100.00 | 100.00 | 100.00 | 100.00 | 100.00 | 100.00 |
| | Facial Distortion | 94.31 | 94.95 | 93.76 | 98.62 | 92.94 | 98.72 | 83.94 | 97.43 |
| Data & Processing | Gaussian Noise | 78.53 | 91.28 | 76.97 | 99.54 | 82.29 | 95.23 | 78.17 | 96.88 |
| | Impulse Noise | 78.72 | 92.29 | 73.49 | 99.27 | 84.59 | 99.08 | 79.17 | 96.42 |
| | Shot Noise | 72.11 | 87.43 | 70.55 | 99.17 | 74.31 | 89.82 | 72.57 | 92.11 |
| | Speckle Noise | 78.44 | 86.88 | 74.68 | 99.08 | 73.03 | 93.03 | 72.29 | 96.79 |
| | Salt Pepper Noise | 63.94 | 89.72 | 54.50 | 98.62 | 69.36 | 97.52 | 63.76 | 72.94 |
| | Jpeg Compression | 97.80 | 98.62 | 97.80 | 100.00 | 100.00 | 100.00 | 100.00 | 100.00 |
| Occlusion | Random Occlusion | 86.06 | 84.86 | 87.25 | 95.96 | 97.52 | 99.54 | 98.62 | 99.82 |
| | Frost | 81.10 | 86.24 | 75.96 | 97.61 | 91.74 | 98.26 | 88.26 | 97.06 |
| | Spatter | 81.65 | 90.55 | 83.76 | 95.23 | 89.45 | 99.82 | 92.11 | 96.51 |
| Average | | 88.32 | 93.77 | 85.44 | 96.89 | 90.91 | 98.38 | 91.29 | 97.15 |

Table H.36. Accuracy of 8 open-source models on Mask-B of corruptions.

| Models | | Mask-C | | | | | | | |
|--------------------|-------------------|---------|------------|---------|---------|-------------|---------|-----------|--------|
| Corruptions | | FaceNet | SphereFace | CosFace | ArcFace | ElasticFace | AdaFace | TransFace | TopoFR |
| None (clean) | | 100.00 | 100.00 | 100.00 | 100.00 | 100.00 | 100.00 | 100.00 | 100.00 |
| Lighting & Weather | Brightness | 100.00 | 100.00 | 100.00 | 100.00 | 100.00 | 100.00 | 100.00 | 100.00 |
| | Contrast | 93.21 | 100.00 | 89.72 | 88.81 | 90.00 | 100.00 | 98.90 | 100.00 |
| | Saturate | 100.00 | 100.00 | 100.00 | 100.00 | 100.00 | 100.00 | 100.00 | 100.00 |
| | Fog | 76.97 | 86.42 | 71.65 | 88.99 | 90.18 | 95.96 | 93.94 | 94.40 |
| | Snow | 88.72 | 94.59 | 89.36 | 99.82 | 98.07 | 99.72 | 97.71 | 99.63 |
| Sensor | Defocus Blur | 89.08 | 88.81 | 70.55 | 80.00 | 80.00 | 100.00 | 98.53 | 100.00 |
| | Color Shift | 100.00 | 100.00 | 100.00 | 100.00 | 100.00 | 100.00 | 100.00 | 100.00 |
| | Pixelate | 100.00 | 100.00 | 99.91 | 100.00 | 100.00 | 100.00 | 100.00 | 100.00 |
| Movement | Motion Blur | 96.24 | 94.95 | 85.32 | 91.65 | 95.23 | 98.62 | 99.54 | 99.91 |
| | Zoom Blur | 97.25 | 100.00 | 100.00 | 100.00 | 100.00 | 100.00 | 100.00 | 100.00 |
| | Facial Distortion | 93.58 | 94.59 | 94.68 | 99.36 | 94.13 | 99.36 | 83.30 | 98.07 |
| Data & Processing | Gaussian Noise | 77.80 | 91.74 | 74.31 | 99.54 | 81.38 | 96.06 | 78.26 | 96.42 |
| | Impulse Noise | 79.36 | 91.38 | 74.22 | 99.72 | 83.30 | 98.81 | 80.37 | 97.43 |
| | Shot Noise | 71.83 | 88.90 | 69.36 | 99.17 | 74.31 | 91.38 | 72.39 | 91.38 |
| | Speckle Noise | 78.17 | 87.34 | 72.20 | 98.90 | 73.12 | 93.12 | 71.93 | 96.51 |
| | Salt Pepper Noise | 64.95 | 87.16 | 53.76 | 99.08 | 69.45 | 97.16 | 65.50 | 73.94 |
| | Jpeg Compression | 97.80 | 98.62 | 97.80 | 100.00 | 100.00 | 100.00 | 100.00 | 100.00 |
| Occlusion | Random Occlusion | 85.23 | 84.86 | 85.41 | 96.79 | 97.25 | 99.36 | 98.90 | 99.91 |
| | Frost | 80.92 | 85.78 | 74.13 | 97.25 | 92.94 | 98.99 | 88.44 | 97.06 |
| | Spatter | 79.08 | 89.36 | 85.14 | 96.79 | 88.44 | 99.91 | 91.10 | 97.52 |
| Average | | 88.10 | 93.55 | 85.12 | 96.95 | 90.85 | 98.50 | 91.37 | 97.25 |

Table H.37. Accuracy of 8 open-source models on Mask-C of corruptions.

| Models | | Mask-D | | | | | | | |
|--------------------|-------------------|---------|------------|---------|---------|-------------|---------|-----------|--------|
| Corruptions | | FaceNet | SphereFace | CosFace | ArcFace | ElasticFace | AdaFace | TransFace | TopoFR |
| None (clean) | | 100.00 | 100.00 | 100.00 | 100.00 | 100.00 | 100.00 | 100.00 | 100.00 |
| Lighting & Weather | Brightness | 100.00 | 100.00 | 100.00 | 100.00 | 100.00 | 100.00 | 100.00 | 100.00 |
| | Contrast | 95.30 | 99.76 | 86.63 | 80.72 | 90.00 | 100.00 | 91.20 | 96.27 |
| | Saturate | 100.00 | 100.00 | 100.00 | 100.00 | 100.00 | 100.00 | 100.00 | 100.00 |
| | Fog | 75.66 | 90.48 | 81.57 | 86.02 | 90.12 | 93.86 | 83.01 | 89.52 |
| | Snow | 92.65 | 93.37 | 97.35 | 99.28 | 98.67 | 99.76 | 87.83 | 95.30 |
| Sensor | Defocus Blur | 85.66 | 79.64 | 77.35 | 83.73 | 80.00 | 100.00 | 91.08 | 100.00 |
| | Color Shift | 100.00 | 100.00 | 100.00 | 100.00 | 100.00 | 100.00 | 100.00 | 100.00 |
| | Pixelate | 99.76 | 100.00 | 100.00 | 100.00 | 100.00 | 100.00 | 99.76 | 100.00 |
| Movement | Motion Blur | 90.72 | 91.20 | 90.24 | 88.67 | 86.87 | 95.78 | 96.87 | 97.95 |
| | Zoom Blur | 99.16 | 100.00 | 100.00 | 100.00 | 99.04 | 100.00 | 92.17 | 96.14 |
| | Facial Distortion | 93.61 | 93.61 | 99.04 | 97.11 | 86.75 | 98.67 | 73.37 | 90.00 |
| Data & Processing | Gaussian Noise | 77.47 | 90.24 | 84.10 | 94.22 | 74.82 | 92.05 | 73.13 | 80.36 |
| | Impulse Noise | 76.87 | 90.48 | 83.86 | 95.42 | 78.67 | 95.78 | 74.94 | 82.29 |
| | Shot Noise | 69.64 | 90.48 | 81.57 | 90.72 | 69.28 | 87.35 | 66.75 | 70.72 |
| | Speckle Noise | 70.84 | 89.40 | 86.87 | 92.29 | 71.81 | 90.24 | 71.20 | 72.41 |
| | Salt Pepper Noise | 62.89 | 90.48 | 60.12 | 89.16 | 63.86 | 91.33 | 54.70 | 57.35 |
| | Jpeg Compression | 99.76 | 100.00 | 100.00 | 100.00 | 100.00 | 100.00 | 100.00 | 100.00 |
| Occlusion | Random Occlusion | 87.83 | 83.49 | 88.92 | 92.29 | 93.73 | 98.31 | 94.46 | 95.66 |
| | Frost | 89.28 | 87.47 | 89.64 | 93.61 | 87.71 | 96.27 | 79.64 | 90.48 |
| | Spatter | 89.40 | 91.33 | 92.05 | 93.37 | 90.12 | 99.88 | 86.87 | 89.28 |
| Average | | 88.41 | 93.40 | 90.44 | 94.13 | 88.64 | 97.11 | 86.52 | 90.65 |

Table H.38. Accuracy of 8 open-source models on Mask-D of corruptions.

| Models | | Mask-E | | | | | | | |
|--------------------|-------------------|---------|------------|---------|---------|-------------|---------|-----------|--------|
| Corruptions | | FaceNet | SphereFace | CosFace | ArcFace | ElasticFace | AdaFace | TransFace | TopoFR |
| None (clean) | | 100.00 | 100.00 | 100.00 | 100.00 | 100.00 | 100.00 | 100.00 | 100.00 |
| Lighting & Weather | Brightness | 99.19 | 98.89 | 100.00 | 100.00 | 100.00 | 100.00 | 100.00 | 100.00 |
| | Contrast | 81.82 | 100.00 | 84.34 | 90.00 | 90.10 | 100.00 | 99.49 | 100.00 |
| | Saturate | 99.39 | 99.90 | 100.00 | 100.00 | 100.00 | 100.00 | 100.00 | 100.00 |
| | Fog | 59.60 | 77.47 | 75.86 | 88.99 | 96.16 | 96.06 | 97.17 | 96.87 |
| Sensor | Snow | 75.35 | 74.14 | 81.01 | 98.69 | 99.09 | 97.07 | 94.65 | 97.47 |
| | Defocus Blur | 83.94 | 65.96 | 67.88 | 86.36 | 89.60 | 93.13 | 94.95 | 100.00 |
| | Color Shift | 98.89 | 96.57 | 99.80 | 100.00 | 100.00 | 100.00 | 100.00 | 100.00 |
| Movement | Pixelate | 87.78 | 77.78 | 99.29 | 100.00 | 100.00 | 100.00 | 99.49 | 99.19 |
| | Motion Blur | 60.51 | 61.31 | 72.83 | 79.70 | 88.38 | 80.81 | 92.53 | 94.04 |
| | Zoom Blur | 67.68 | 75.35 | 86.46 | 95.25 | 79.60 | 87.07 | 93.64 | 94.85 |
| Data & Processing | Facial Distortion | 80.00 | 71.01 | 92.12 | 94.44 | 92.12 | 86.06 | 76.77 | 88.69 |
| | Gaussian Noise | 65.66 | 83.74 | 84.14 | 98.89 | 87.37 | 98.08 | 82.93 | 87.58 |
| | Impulse Noise | 65.56 | 83.43 | 82.02 | 98.79 | 90.71 | 96.67 | 84.34 | 90.20 |
| | Shot Noise | 65.15 | 75.66 | 79.90 | 96.77 | 82.42 | 94.95 | 78.69 | 84.95 |
| | Speckle Noise | 73.43 | 72.93 | 84.75 | 98.89 | 91.41 | 97.07 | 82.02 | 93.54 |
| | Salt Pepper Noise | 58.28 | 79.09 | 63.33 | 94.95 | 80.40 | 92.32 | 65.56 | 74.75 |
| | Jpeg Compression | 91.21 | 89.70 | 97.17 | 99.80 | 100.00 | 98.99 | 98.59 | 99.70 |
| Occlusion | Random Occlusion | 77.88 | 68.99 | 81.01 | 85.35 | 92.12 | 89.39 | 93.94 | 93.74 |
| | Frost | 71.41 | 77.17 | 84.95 | 96.46 | 97.78 | 97.98 | 92.32 | 97.37 |
| | Spatter | 79.60 | 82.02 | 88.48 | 97.37 | 98.28 | 98.59 | 95.35 | 96.36 |
| Average | | 78.21 | 81.48 | 85.97 | 95.27 | 93.12 | 95.44 | 91.54 | 94.73 |

Table H.39. Accuracy of 8 open-source models on Mask-E of corruptions.

| Models | | Mask-A | | | | | | | |
|-------------------|----------------|---------|------------|---------|---------|-------------|---------|-----------|--------|
| Variations | | FaceNet | SphereFace | CosFace | ArcFace | ElasticFace | AdaFace | TransFace | TopoFR |
| None (clean) | | 100.00 | 100.00 | 100.00 | 100.00 | 100.00 | 100.00 | 100.00 | 100.00 |
| Age | Age- | 100.00 | 66.33 | 100.00 | 100.00 | 100.00 | 100.00 | 100.00 | 100.00 |
| | Age+ | 100.00 | 64.00 | 100.00 | 100.00 | 100.00 | 100.00 | 100.00 | 100.00 |
| Facial Expression | Mouth-close | 100.00 | 50.00 | 100.00 | 100.00 | 100.00 | 100.00 | 100.00 | 100.00 |
| | Mouth-open | 100.00 | 59.33 | 99.00 | 100.00 | 100.00 | 100.00 | 100.00 | 100.00 |
| | Eye-close | 100.00 | 79.00 | 100.00 | 100.00 | 100.00 | 100.00 | 100.00 | 100.00 |
| | Eye-open | 100.00 | 50.00 | 88.00 | 100.00 | 100.00 | 100.00 | 100.00 | 100.00 |
| Rotation | Rotation-left | 100.00 | 50.00 | 100.00 | 100.00 | 100.00 | 100.00 | 100.00 | 100.00 |
| | Rotation-right | 100.00 | 72.67 | 100.00 | 100.00 | 100.00 | 100.00 | 100.00 | 100.00 |
| Accessories | Hair&Glasses | 100.00 | 86.33 | 100.00 | 100.00 | 100.00 | 100.00 | 100.00 | 100.00 |
| | Makeup | 100.00 | 88.00 | 100.00 | 100.00 | 100.00 | 100.00 | 100.00 | 100.00 |
| Average | | 100.00 | 69.61 | 98.82 | 100.00 | 100.00 | 100.00 | 100.00 | 100.00 |

Table H.40. Accuracy of 8 open-source models on Mask-A of variations.

| Models | | Mask-B | | | | | | | |
|-------------------|----------------|---------|------------|---------|---------|-------------|---------|-----------|--------|
| Variations | | FaceNet | SphereFace | CosFace | ArcFace | ElasticFace | AdaFace | TransFace | TopoFR |
| None (clean) | | 100.00 | 100.00 | 100.00 | 100.00 | 100.00 | 100.00 | 100.00 | 100.00 |
| Age | Age- | 100.00 | 81.56 | 99.72 | 100.00 | 100.00 | 100.00 | 100.00 | 100.00 |
| | Age+ | 100.00 | 98.99 | 100.00 | 100.00 | 100.00 | 100.00 | 100.00 | 100.00 |
| Facial Expression | Mouth-close | 100.00 | 82.75 | 100.00 | 99.72 | 100.00 | 100.00 | 100.00 | 100.00 |
| | Mouth-open | 100.00 | 96.42 | 99.91 | 100.00 | 100.00 | 100.00 | 100.00 | 100.00 |
| | Eye-close | 100.00 | 100.00 | 100.00 | 100.00 | 100.00 | 100.00 | 100.00 | 100.00 |
| | Eye-open | 100.00 | 63.58 | 99.54 | 100.00 | 100.00 | 100.00 | 100.00 | 100.00 |
| Rotation | Rotation-left | 100.00 | 89.82 | 100.00 | 100.00 | 100.00 | 100.00 | 100.00 | 100.00 |
| | Rotation-right | 100.00 | 96.70 | 100.00 | 100.00 | 100.00 | 100.00 | 100.00 | 100.00 |
| Accessories | Hair&Glasses | 100.00 | 86.42 | 96.15 | 100.00 | 100.00 | 100.00 | 100.00 | 100.00 |
| | Makeup | 100.00 | 94.22 | 100.00 | 100.00 | 100.00 | 100.00 | 100.00 | 100.00 |
| Average | | 100.00 | 90.04 | 99.57 | 99.97 | 100.00 | 100.00 | 100.00 | 100.00 |

Table H.41. Accuracy of 8 open-source models on Mask-B of variations.

| Models | | Mask-C | | | | | | | |
|-------------------|----------------|---------|------------|---------|---------|-------------|---------|-----------|--------|
| Variations | | FaceNet | SphereFace | CosFace | ArcFace | ElasticFace | AdaFace | TransFace | TopoFR |
| None (clean) | | 100.00 | 100.00 | 100.00 | 100.00 | 100.00 | 100.00 | 100.00 | 100.00 |
| Age | Age- | 100.00 | 59.15 | 53.22 | 100.00 | 100.00 | 100.00 | 99.15 | 100.00 |
| | Age+ | 100.00 | 98.31 | 99.49 | 100.00 | 100.00 | 100.00 | 100.00 | 100.00 |
| Facial Expression | Mouth-close | 100.00 | 61.53 | 90.17 | 92.37 | 100.00 | 100.00 | 99.66 | 99.66 |
| | Mouth-open | 100.00 | 85.08 | 80.17 | 100.00 | 100.00 | 100.00 | 100.00 | 100.00 |
| | Eye-close | 100.00 | 96.78 | 94.92 | 100.00 | 100.00 | 100.00 | 100.00 | 100.00 |
| | Eye-open | 100.00 | 55.42 | 58.64 | 100.00 | 100.00 | 100.00 | 100.00 | 100.00 |
| Rotation | Rotation-left | 100.00 | 66.78 | 76.10 | 100.00 | 100.00 | 100.00 | 100.00 | 100.00 |
| | Rotation-right | 100.00 | 88.14 | 91.53 | 100.00 | 100.00 | 100.00 | 100.00 | 100.00 |
| Accessories | Hair&Glasses | 100.00 | 99.32 | 100.00 | 100.00 | 100.00 | 100.00 | 100.00 | 100.00 |
| | Makeup | 100.00 | 79.83 | 100.00 | 100.00 | 100.00 | 100.00 | 100.00 | 100.00 |
| Average | | 100.00 | 80.94 | 85.84 | 99.31 | 100.00 | 100.00 | 99.89 | 99.97 |

Table H.42. Accuracy of 8 open-source models on Mask-C of variations.

| Models | | Mask-D | | | | | | | |
|-------------------|----------------|---------|------------|---------|---------|-------------|---------|-----------|--------|
| Variations | | FaceNet | SphereFace | CosFace | ArcFace | ElasticFace | AdaFace | TransFace | TopoFR |
| None (clean) | | 100.00 | 100.00 | 100.00 | 100.00 | 100.00 | 100.00 | 100.00 | 100.00 |
| Age | Age- | 95.78 | 57.35 | 97.59 | 97.71 | 99.52 | 100.00 | 99.76 | 100.00 |
| | Age+ | 100.00 | 77.71 | 100.00 | 100.00 | 100.00 | 100.00 | 100.00 | 100.00 |
| Facial Expression | Mouth-close | 99.88 | 53.01 | 98.92 | 84.82 | 99.28 | 100.00 | 100.00 | 99.64 |
| | Mouth-open | 100.00 | 74.70 | 99.76 | 100.00 | 100.00 | 100.00 | 100.00 | 100.00 |
| | Eye-close | 99.52 | 89.28 | 100.00 | 97.59 | 100.00 | 100.00 | 100.00 | 99.52 |
| | Eye-open | 100.00 | 53.25 | 94.46 | 100.00 | 100.00 | 100.00 | 100.00 | 100.00 |
| Rotation | Rotation-left | 100.00 | 67.71 | 99.88 | 100.00 | 100.00 | 100.00 | 100.00 | 100.00 |
| | Rotation-right | 100.00 | 67.83 | 100.00 | 99.76 | 100.00 | 100.00 | 100.00 | 100.00 |
| Accessories | Hair&Glasses | 100.00 | 93.73 | 98.43 | 100.00 | 100.00 | 100.00 | 100.00 | 100.00 |
| | Makeup | 100.00 | 84.46 | 100.00 | 100.00 | 100.00 | 100.00 | 100.00 | 100.00 |
| Average | | 99.56 | 74.46 | 99.00 | 98.17 | 99.89 | 100.00 | 99.93 | 99.97 |

Table H.43. Accuracy of 8 open-source models on Mask-D of variations.

| Models | | Mask-E | | | | | | | |
|-------------------|----------------|---------|------------|---------|---------|-------------|---------|-----------|--------|
| Variations | | FaceNet | SphereFace | CosFace | ArcFace | ElasticFace | AdaFace | TransFace | TopoFR |
| None (clean) | | 100.00 | 100.00 | 100.00 | 100.00 | 100.00 | 100.00 | 100.00 | 100.00 |
| Age | Age- | 50.00 | 50.00 | 66.06 | 89.49 | 99.80 | 87.27 | 99.80 | 100.00 |
| | Age+ | 91.92 | 50.00 | 61.01 | 82.02 | 99.80 | 77.68 | 97.37 | 93.94 |
| Facial Expression | Mouth-close | 50.00 | 50.00 | 64.95 | 58.59 | 93.54 | 66.16 | 91.01 | 94.55 |
| | Mouth-open | 92.73 | 50.00 | 68.38 | 89.09 | 99.39 | 69.60 | 99.29 | 95.66 |
| | Eye-close | 51.31 | 50.40 | 65.25 | 88.59 | 100.00 | 69.80 | 100.00 | 100.00 |
| | Eye-open | 62.83 | 50.00 | 57.88 | 86.06 | 100.00 | 83.94 | 100.00 | 100.00 |
| Rotation | Rotation-left | 51.41 | 50.00 | 59.29 | 81.31 | 95.45 | 73.03 | 99.39 | 99.60 |
| | Rotation-right | 59.49 | 50.00 | 67.07 | 87.78 | 99.70 | 78.28 | 98.28 | 100.00 |
| Accessories | Hair&Glasses | 93.64 | 56.67 | 82.22 | 98.79 | 100.00 | 83.23 | 99.09 | 100.00 |
| | Makeup | 80.40 | 51.52 | 81.92 | 100.00 | 100.00 | 99.70 | 100.00 | 100.00 |
| Average | | 71.25 | 55.33 | 70.37 | 87.43 | 98.88 | 80.79 | 98.57 | 98.52 |

Table H.44. Accuracy of 8 open-source models on Mask-E of variations.